

# DISSECTING THE QUADRUPLE BINARY HYAD vA 351 - MASSES FOR THREE M DWARFS AND A WHITE DWARF

G. FRITZ BENEDICT

McDonald Observatory, University of Texas, Austin, TX 78712

OTTO G. FRANZ

Lowell Observatory, 1400 West Mars Hill Rd., Flagstaff, AZ 86001

ELLIOTT P. HORCH

Southern Connecticut State University, New Haven, CT 06515

L. PRATO

Lowell Observatory, 1400 West Mars Hill Rd., Flagstaff, AZ 86001

GUILLERMO TORRES

Center for Astrophysics | Harvard & Smithsonian, Cambridge MA 02138

BARBARA E. MCARTHUR

McDonald Observatory, University of Texas, Austin, TX 78712

LAWRENCE H. WASSERMAN

Lowell Observatory, 1400 West Mars Hill Rd., Flagstaff, AZ 86001

DAVID W. LATHAM

Center for Astrophysics | Harvard & Smithsonian, Cambridge MA 02138

ROBERT P. STEFANIK

Center for Astrophysics | Harvard & Smithsonian, Cambridge MA 02138

CHRISTIAN LATHAM

Center for Astrophysics | Harvard & Smithsonian, Cambridge MA 02138

BRIAN A. SKIFF

Lowell Observatory, 1400 West Mars Hill Rd., Flagstaff, AZ 86001

(Received; Revised; Accepted)  
*Draft version April 8, 2021*

## ABSTRACT

We extend results first announced by Franz et al. (1998), that identified vA 351 = H346 in the Hyades as a multiple star system containing a white dwarf. With Hubble Space Telescope Fine Guidance Sensor fringe tracking and scanning, and more recent speckle observations, all spanning 20.7 years, we establish a parallax, relative orbit, and mass fraction for two components, with a period,  $P = 2.70$ y and total mass  $2.1M_{\odot}$ . With ground-based radial velocities from the McDonald Observatory Otto Struve 2.1m telescope Sandiford Spectrograph, and Center for Astrophysics Digital Speedometers, spanning 37 years, we find that component B consists of BC, two M dwarf stars orbiting with a very short period ( $P_{BC} = 0.749$  days), having a mass ratio  $M_C/M_B=0.95$ . We confirm that the total mass of the system can only be reconciled with the distance and component photometry by including a fainter, higher mass component. The quadruple system consists of three M dwarfs (A,B,C) and one white dwarf (D). We determine individual M dwarf masses  $M_A=0.53\pm0.10M_{\odot}$ ,  $M_B=0.43\pm0.04M_{\odot}$ , and  $M_C=0.41\pm0.04M_{\odot}$ . The WD mass,  $0.54\pm0.04M_{\odot}$ , comes from cooling models, an assumed Hyades age of 670My, and consistency with all previous and derived astrometric, photometric, and RV results. Velocities from H $\alpha$  and He I emission lines confirm the BC period derived

<sup>1</sup> We dedicate this paper to John Stauffer, who died on 2021

January 29, in honor of his many contributions to the field.

from absorption lines, with similar (He I) and higher (H $\alpha$ ) velocity amplitudes. We ascribe the larger H $\alpha$  amplitude to emission from a region each component shadows from the other, depending on the line of sight.

*Subject headings:* astrometry — interferometry — stars: binary — stars: radial velocities — stars: late-type — stars: distances — stars: masses

## 1. INTRODUCTION

The Hyades, an open cluster whose every member contributes to our knowledge of stellar evolution, open cluster formation, and open cluster evolution, remains an important rung on the extragalactic distance scale ladder (An *et al.* 2007; de Bruijne *et al.* 2001). Much effort has resulted in an ever improving Hyades distance, from convergent point methods (van Bueren 1952; Hanson 1975) using only proper motions, to directly measured parallax (Perryman *et al.* 1998; McArthur *et al.* 2011), through recent efforts using a combination of parallax, proper motion, and radial velocities (Gaia Collaboration *et al.* 2017), with cluster membership determination always a critical issue. Hence the first goal of this project is an unambiguous determination of cluster membership for vA 351=H346 = L42 = V805 Tau = HG7-203 = LP415-65, RA 04<sup>h</sup>25<sup>m</sup>13.54<sup>s</sup> DEC +17°16′05″.48 (2000), V=13.27, K=8.27.

This Hyad was first angularly resolved (Franz *et al.* 1994) as a result of a blind search of faint members of the Hyades, using the *Hubble Space Telescope* (*HST*) Fine Guidance Sensor #3 (*FGS3*) in the transfer function or fringe scanning (TRANS) mode. Franz *et al.* (1998a) details this *FGS* observation mode. Further observations yielded a relative orbit, and, depending on an assumed parallax based on Hyades membership, a total mass for the system (Franz *et al.* 1998b) inconsistent with the colors and spectral types suggesting M dwarf components. A white dwarf component was posited to bring the total mass into agreement with the dynamical mass. Subsequently, we acquired *FGS3* POS mode observations (the fringe tracking POS mode described in Benedict *et al.* 2016) with which to derive a mass fraction and independent parallax. Once vA 351 was identified as a binary we added it to our then ongoing Mass-Luminosity Relation radial velocity program, also described in Benedict *et al.* (2016). Thus our second goal: to establish the physical properties of all vA 351 components, determining how many stars comprise this system, and derive their individual component masses.

Observational astronomers are hard-pressed to devise experiments. Nature provides these by presenting us with binary stars. Put one star next to another and see what happens. Extreme cases provide laboratories within which to test our knowledge of stellar magnetic fields and mass transfer. vA 351 provides such a laboratory. Hence, a detailed examination of the complex behavior of a subset of vA 351 components provides a third goal, that of generating a qualitative model explaining the observations.

These observations include *FGS* TRANS which use the entire fringe to match a superposition of the fringe of each component to the fringe of a known single star, resulting in position angles and separations with which to derive a relative orbit. They also provide component magnitude

differences. *FGS* POS mode produces positions of the zero crossing of a fringe for each star observed. Measuring a series of vA 351 positions relative to a known reference frame provides a parallax, establishes a proper motion for the center of mass of the system, and yields a mass ratio for the supposed two components. For many of the M dwarf binary systems investigated in Benedict *et al.* (2016), adding radial velocities (RVs) to the astrometry allowed us to completely sample the motion of a binary system. The three complementary data sets improve the accuracies of the final component masses. For vA 351 all assist in dissecting the system, yielding masses for the four components.

This paper summarizes our efforts to understand the vA 351 system. We first present the results of our analysis of the TRANS-mode astrometric data, yielding a binary orbit and total mass (Section 2). Next we present a radial velocity (RV) analysis using absorption lines, yielding a  $\mathcal{M}_C/\mathcal{M}_B$  mass ratio (Section 3) and a confirmation of the component A RVs with respect to the AD-BC barycenter. Finally we fold in the POS-mode data and derive a mass fraction, a proper motion, and a parallax for the system (Section 4). Section 5 presents evidence of small amplitude but precisely measured variability from photometry acquired with the POS mode observations, and recent ground-based *V*-band photometry. In Section 6 we use to these results to confirm masses for the three M dwarf components and to derive a WD mass required to satisfy the derived total mass and the  $(\mathcal{M}_A+\mathcal{M}_D)/(\mathcal{M}_B+\mathcal{M}_C)$  mass ratio. Half our spectra include emission lines of both H $\alpha$  and He I ( $\lambda 5876.6\text{\AA}$ ). We derive equivalent widths and RVs for both H $\alpha$  and He I emission lines (Section 7). We describe the structure of this quadruple system and posit some possible emission line formation mechanisms (Section 8), offer conclusions (Section 9), and summarize our results in Section 10.

Unless otherwise noted, times are modified Julian Date, mJD = JD-2400000.5. We abbreviate millisecond of arc as mas throughout.

## 2. THE vA 351 RELATIVE ORBIT

We have 13 position angle and separation TRANS mode measurements of component B relative to component A acquired over 4.7 yr. Five speckle measures, taken with the DSSI speckle camera on the 4.3m Lowell Observatory Discovery Telescope (LDT; formerly DCT), extend the relative orbit astrometric coverage to 26.0 yr. The LDT speckle program (Horch *et al.* 2012, 2015), in operation since 2014, obtained data for vA 351 on four separate nights in October and November of that year. A more recent observation, under very poor weather conditions, was secured in early February 2020. Analysis of these data files proceeded using the same methodology as described most recently in Horch *et al.* (2017), using a weighted least-squares fit to the summed spatial frequency power spectrum of the speckle data frames.

We transformed all position angle and separation observations into  $x$  and  $y$  positions and assigned a 1.5 mas error to each  $x$ ,  $y$ , this to yield a reduced  $\chi^2$  near unity for the relative orbit modeling. Figure 1 contains the resulting low-inclination, high eccentricity relative orbit with observations and residuals presented in Table 1 and orbital parameters listed in Table 2. The second largest residual in Figure 1 (#18) comes from the February 2020 speckle measurement, secured under very poor weather conditions. We excluded this and one early TRANS observation (#2, components unresolved along one *FGS* axis) in the final orbit determination.

The relative orbit appears quite plausible. However, see the Appendix for an arduous and tortuous path traversed, and for a blind alley out of which we backed, to eventually arrive at Figure 1.

### 3. ABSORPTION-LINE SPECTROSCOPY

#### 3.1. McDonald Cassegrain Echelle Spectrograph

We obtained RV data with the McDonald 2.1m Otto Struve telescope and Sandiford Cassegrain Echelle spectrograph (McCarthy et al. 1993), hereafter CE. The CE delivers a dispersion equivalent to  $2.5 \text{ km s}^{-1}/\text{pix}$  ( $R = \lambda/\Delta\lambda = 60,000$ ) with a wavelength range of  $5500 \leq \lambda \leq 6700 \text{ \AA}$  spread across 26 orders. The McDonald data were collected during thirty-three observing runs from 1995 to 2009 and reduced using the standard IRAF (Tody 1993) *echelle* package tools. CE RVs (listed in Table 3) were derived using the IRAF cross-correlation tool *fxcorr*.

#### 3.2. Center for Astrophysics Digital Speedometers

vA 351 was monitored spectroscopically at the CfA with the Digital Speedometers (Latham 1992) between January of 1982 and October of 1999, on two telescopes: the 1.5m Tillinghast reflector at the Fred L. Whipple Observatory on Mount Hopkins (AZ), and the 4.5m-equivalent Multiple Mirror Telescope (also on Mount Hopkins) before its conversion to a monolithic 6.5m telescope. With a resolving power,  $R \approx 35,000$ , the spectra consist of a single echelle order centered on the Mg I b triplet (5187 Å) and spanning 45 Å. Reductions were carried out with a dedicated pipeline. The average signal-to-noise ratio for the 53 observations is about 12 per resolution element of  $8.5 \text{ km s}^{-1}$ . We identify this source as CfA, hereafter, and provide the CfA RVs in Table 4.

#### 3.3. IGRINS and other Sources of vA 351 RVs

On UT 2016 February 23 and 25 we obtained two epochs with the  $R=45,000$ , near-infrared spectrograph IGRINS (Mace et al. 2016) on the McDonald Observatory Harlan J. Smith 2.7m telescope. An additional observation was taken on UT 2019 April 11 at the 4.3m LDT. Exposure times were 16–24 minutes, divided into 2 or 4 nodded pairs at two distinct slit positions. The resulting signal to noise was  $>100$  per resolution element of  $\sim 6 \text{ km s}^{-1}$ . Data reduction was carried out using standard processing with the IGRINS pipeline (Lee et al. 2017)<sup>1</sup>. The pipeline yields telluric-corrected, one-dimensional spectra with wavelength dispersion solutions

determined from OH night sky emission lines and atmospheric absorption lines. Barycentric velocity corrections were applied to the target and RV standard star data as part of the cross-correlation analysis (Section 3.4).

Hartmann et al. (1987) report a single RV of (presumably) component A with the MMT. Stauffer et al. (1997) present two RV measurements of vA 351 components A, B, and C obtained with the NOAO 4m Mayall telescope at two epochs separated by  $\sim 50$  days. We list dates, RVs, and phases for these three epochs from the literature and the three IGRINS epochs in Table 5.

#### 3.4. Absorption Line Analysis

For the CE observations we used the same high-resolution, high signal-to-noise template spectrum of GJ623 AB as in Benedict et al. (2016) for all absorption line cross-correlations. The quality of the GJ623 AB orbit yields an absolute RV uncertainty at the epoch of template observation of less than  $0.025 \text{ km s}^{-1}$  (Benedict et al. 2016, table 4). GJ623 AB has a  $\Delta V = 5.2$ , rendering the effect of the secondary on the cross-correlation function (CCF) negligible. We visually inspected the resulting CCF to select the better of the 26 apertures, typically using half to obtain an average velocity. The CCF resulting from the absorption line template had from one to three peaks (Table 3), indicating the existence of at least three, not just two components (hereafter, components A, B, and C). We identify component A with the strongest peak in the CCF, and list all CE component RVs with internal  $1 - \sigma$  errors in Table 3. For components A, B, and C we find average internal per epoch errors; 0.3, 0.6, and  $0.8 \text{ km s}^{-1}$ .

Radial velocities from the CfA and IGRINS spectra were measured with algorithms for three-dimensional cross-correlation such as TRICOR (Zucker et al. 1995). For the IGRINS data, we used the same template for the three vA 351 components (A, B, and C), a high S/N exposure of the slowly rotating M2 star GJ 725A (Prato 2007; Mann et al. 2015). For the CfA data, rotational broadening was applied to achieve the best overall match, resulting in  $v \sin i$  estimates of  $11 \pm 2 \text{ km s}^{-1}$  for stars B and C, and  $3 \pm 3 \text{ km s}^{-1}$  for the brighter star A. For the IGRINS observations, the cross-correlation coefficient was optimized when we used the GJ 752A template for the A component, with no broadening applied, and the M2.5 dwarf standard GJ 436 for the B and C components with  $v \sin i$  of  $12 \pm 2 \text{ km s}^{-1}$  (Prato 2007; Mann et al. 2015). For both the optical and IR data, these  $v \sin i$  values agree with the independent determinations of Stauffer et al. (1997).

From CfA measurements the light ratio of each of the fainter components relative to star A was found to be  $0.53 \pm 0.02$  at the mean wavelength of these observations. This yields a flux ratio  $BC/AD = 1.06 \pm 0.03$ , or  $\Delta m = 0.06 \pm 0.03$ , with BC being marginally brighter at this wavelength. The bandpass is somewhat close to V though on the blue side and much narrower (45 Å). It is similar to the D51 filter used for the Kepler Input Catalog (Brown et al. 2011), which was modeled after the Dunlap Observatory DDO51 filter. The CfA  $\Delta m = 0.06 \pm 0.03$  is consistent with the measurements listed in Table 1. The IGRINS *H*-band spectra yielded light ratios of  $B/A=0.66 \pm 0.02$  and  $C/A=0.64 \pm 0.08$ , hence a  $BC/AD$  flux ratio of  $1.3 \pm 0.1$  and  $\Delta H = 0.28$  (combined

<sup>1</sup> <https://github.com/igrins/plp/tree/v2.1-alpha.3>

components AD fainter than combined components BC), a puzzle given the  $V$ - and  $K$ -band lower  $\Delta m$  values (Table 1).

The two fainter components, B and C, exhibit the largest RV variation. When fit to an orbit these yield the elements listed in Table 6. We plot component velocities phased to a BC period,  $P_{BC} = 0.7492425^d$  in Figure 2. The rms RV residual to these orbits is  $2.7 \text{ km s}^{-1}$ . A ratio of the RV amplitudes yields a mass ratio for components C and B;  $K_B/K_C = \mathcal{M}_C/\mathcal{M}_B = 0.945 \pm 0.005$ . The average component A RV is  $\langle V_A \rangle = +40.7 \pm 2.0 \text{ km s}^{-1}$ . An average of the BC RV  $\gamma$  values yields  $\langle V_{BC} \rangle = +40.2 \pm 0.2 \text{ km s}^{-1}$ . We have consistency with the expected radial velocity of a Hyades member at the location of vA 351,  $V = +39.80 \text{ km s}^{-1}$ , computed from a convergent point solution with the location of the convergent point as reported by the Gaia Collaboration *et al.* (2017) ( $\alpha_{J2000} = 97^\circ 73$ ,  $\delta_{J2000} = +6^\circ 83$ ), adopting a space velocity for the cluster of  $V_0 = +47.13 \text{ km s}^{-1}$ , based on ongoing radial velocity measurements at the CfA.

In Figure 3 we plot the RV variation attributable to the motion of A about a common center of mass with BC, phased to the period (Table 7) determined through a solution incorporating only RVs. While noisy, the component A velocities show a clear signature of a highly eccentric orbit. We were unable to extract a clear signature of the BC center of mass motions around the AD-BC system barycenter.

#### 4. POS MODE ASTROMETRY

Benedict *et al.* (2016) describes the acquisition and reduction of *FGS* POS mode data. Figure 4 shows the distribution on the sky of the four reference stars (numbers 2, 3, 4, 5) for the POS mode measurements, with number 1 indicating vA 351. Not all reference stars were measured at each of the seven epochs of observation that included POS mode. We acquired all *HST* astrometry data sets with *FGS3*. For POS mode we obtained a total of 50 reference star observations and 19 observations of vA 351, secured over 1.8 years.

##### 4.1. Prior Knowledge and Modeling Constraints

As in our previous astrometry projects, *e.g.*, Benedict *et al.* (2001, 2007, 2011); McArthur *et al.* (2011); Benedict *et al.* (2016) we include as much prior information as possible in our *FGS* fringe-tracking modeling. In contrast to much of our previous relative astrometry (*e.g.*, Harrison *et al.* 1999, Benedict *et al.* 2011), for this project we obtain reference star absolute parallaxes and proper motion priors from *Gaia* DR2 (Gaia Collaboration *et al.* 2018). A comparison of the Figure 5 color-color diagram with the Table 8 input parallaxes confirms the giant nature of reference stars 4 and 5, labeled ref-4 and ref-5 in the figure.

We did not simply adopt the *Gaia* DR2 parallax for vA 351 because the *Gaia* astrometry does not yet account for over 80 mas (Franz *et al.* 1998b) of orbital motion. Similarly, rather than using the highly precise *Gaia* DR2 proper motion from measures taken over a limited multiple of the AD - BC orbit, we introduce no vA 351 proper motion priors.

In a quasi-Bayesian approach we input all priors as observations with associated errors, not as hardwired quan-

ties known to infinite precision. The lateral color calibration (see section 3.4 of Benedict *et al.* 1999) and the  $B - V$  color indices are also treated as observations with error. <sup>i</sup>

##### 4.2. vA 351 POS Mode Photocenter Corrections

*FGS* POS mode measures the zero-crossing of a fringe. Thus, for a binary the observed fringe becomes a linear superposition of two fringes. For a nearly equal brightness component binary (Table 1) the measured zero crossing can be significantly perturbed from a position coincident with either component. Benedict *et al.* (2001), section 4.2, discusses the generation of such corrections at some length. Figure 6 demonstrates the determination of corrections along the  $x$  and  $y$  axes of *FGS3* for a typical POS mode observation of vA 351. Corrections ranged from 4 mas to 80 mas, the latter required because for that observation the *FGS* locked on the other component.

##### 4.3. The POS Model

From the reference star astrometric data we determine the rotation and offset “plate constants” relative to an arbitrarily adopted constraint epoch (the so-called “master plate”) for each observation set. The vA 351 reference frame contains five stars, but only three were observed at each epoch. Hence, we constrain the scales along  $x$  and  $y$  to that provided by the *FGS* Optical Field Angle Distortion calibration (Benedict *et al.* 1999), and the two axes to orthogonality. The consequences of this choice are minimal. For example, imposing these constraints on the Barnard’s Star astrometry discussed in Benedict *et al.* (1999) results in an unchanged parallax and increases the error by 0.1 mas, compared to a full 6 parameter model (*e.g.* Benedict *et al.* 2017, equations 6,7).

Our reference frame model becomes, in terms of standard coordinates,

$$x' = x + lc_x(B - V) \quad (1)$$

$$y' = y + lc_y(B - V) \quad (2)$$

$$x'' = x' + corr_x \quad (3)$$

$$y'' = y' + corr_y \quad (4)$$

$$\xi = \cos(A) * x'' + \sin(A) * y'' + C - \mu_\alpha \Delta t - P_\alpha \varpi - ORB_\alpha \quad (5)$$

$$\eta = -\sin(A) * x'' + \cos(A) * y'' + F - \mu_\delta \Delta t - P_\delta \varpi - ORB_\delta \quad (6)$$

, where  $x$  and  $y$  are the measured coordinates from *HST*,  $corr_x$  and  $corr_y$  are the photocenter corrections derived in Section 4.2 above,  $lc_x$  and  $lc_y$  are lateral color corrections, and  $B - V$  represents the color of each star, either from SIMBAD or estimated from the spectral types suggested by Figure 5.  $A$  is a field rotation in radians,  $C$  and  $F$  are offsets,  $\mu_\alpha$  and  $\mu_\delta$  are proper motions,  $\Delta t$  is the epoch difference from the mean epoch,  $P_\alpha$  and  $P_\delta$  are parallax factors, and  $\varpi$  is the parallax.  $\xi$  and  $\eta$  are relative positions that (once rotation, parallax, the proper motions are determined) should not change with time. All Equation 5 and 6 subscripts are in RA and DEC because the master constraint plate was rolled into the RA DEC coordinate system before the analysis. We obtain the parallax factors from a JPL Earth orbit predictor

(Standish 1990), upgraded to version DE405. We obtain orientation to the sky for the master plate using ground-based astrometry from the PPMXL (Roeser et al. 2010) with uncertainties in the field orientation of  $\pm 0^\circ.1$ . This orientation also enters the modeling as an observation with error.

We derive  $A$ ,  $C$ , and  $F$  for each epoch only from reference star measurements. Applied as constants, we solve for a position within our reference frame, a parallax, a proper motion, and a major axis measurement,  $\alpha_A$ , for the vA 351A orbit about the system center of mass. To vA 351 we apply *ORB* as a correction term that is a function of the traditional astrometric and RV orbital elements listed in Tables 2 and 7. These include the orbital period ( $P$ ), the epoch of passage through periastron in modified Julian days ( $T_0$ ), the eccentricity ( $e$ ), the inclination,  $i$ , and the position angle of the line of nodes ( $\Omega$ ). We also constrain the angle ( $\omega$ ) in the plane of the true orbit between the line of nodes and the major axis to differ by  $180^\circ$  for the component A and B orbits.

#### 4.4. Assessing Reference Frame Residuals

From histograms of the astrometric residuals for 50 reference star and 19 vA 351 position measurements (Figure 7), we conclude that we have obtained corrections at the 1.2 mas level in the region available at all *HST* roll angles (an inscribed circle centered on the pickle-shaped *FGS* field of regard). The resulting reference frame “catalog” in  $\xi$  and  $\eta$  standard coordinates (Equations 5 and 6) was determined with median absolute errors of  $\sigma_\xi = 0.9$  and  $\sigma_\eta = 1.0$  mas in  $x$  and  $y$ , respectively.

#### 4.5. Results of vA 351 Modeling

In Table 9 we list our final values for the absolute parallax and proper motion (with  $1\sigma$  errors), where the *Gaia* parallaxes from both DR2 and EDR3 (Lindgren et al. 2020) are also included for comparison. We included neither parallax as a prior. Extending the *Gaia* observational time baseline has brought their parallax closer to our value, now only slightly more than  $1\sigma$  different. Stassun & Torres (2021) find that the *Gaia* *RUWE* (renormalised unit weight error) robustly predicts unmodeled photocenter motion, even in the nominal “good” range of 1.0–1.4 (see also Belokurov et al. 2020). For vA 351 EDR3 lists a value very much larger, *RUWE*=9.33, clearly indicating the *Gaia* astrometry was affected. The median *RUWE* value for the 9 stars (with a *Gaia*  $G$ -band magnitude  $G < 16$ , not used as astrometric reference stars) in EDR3 within  $7'$  of vA 351 is 1.05. Reference stars (Table 8) have a median *RUWE* value of 1.38, a partial explanation for our poorer than average (see the 105 parallax results in Benedict et al. 2017) parallax result for vA 351.

Table 10 contains the final orbital parameters with formal ( $1\sigma$ ) uncertainties. Figure 8 illustrates component A and B astrometric orbits. That the *FGS* POS measures did not sample the entire orbit and that the *Gaia* solution thus far neglects orbital motion could provide a partial explanation for the proper motion discrepancies seen in Table 9. The TRANS and speckle astrometric residuals (Table 1, RMS=2.8 mas) suggest an unmodeled perturbation to the TRANS measured separation between components A and B. We discuss further evidence for this perturbation in Section 6.

In the past (e.g. Benedict et al. 2016) we have employed a relationship between astrometry and RV (c.f. Pourbaix & Jorissen 2000) to narrow the range of possible combinations of parallax,  $\varpi$ , and orbit semi-major axis,  $\alpha$ :

$$\frac{\alpha_A \sin i}{\varpi_{\text{abs}}} = \frac{PK_A \sqrt{(1 - \epsilon^2)}}{2\pi \times 4.7405} \quad (7)$$

However, the significant inclination error (Table 2) renders this constraint less useful. The right hand (RHS) and left hand (LHS) quantities calculated from results listed in Tables 2, 7, and 9 do agree within their errors (RHS=  $0.267 \pm 0.154$ , LHS=  $0.220 \pm 0.004$ ).

#### 4.6. vA 351 Component Masses

Our orbit solution and derived absolute parallax provide an orbital semimajor axis,  $a$  in AU, from which we can determine the system mass through Kepler’s Third Law. We find (in solar units)  $\mathcal{M}_{\text{tot}} = 2.06 \pm 0.24 \mathcal{M}_\odot$ . At each instant in the orbits of the two components around the common center of mass,

$$\mathcal{M}_A / \mathcal{M}_B = \alpha_B / \alpha_A \quad (8)$$

a relationship that contains only one observable,  $\alpha_A$ , the vA 351 semi-major axis measurement. Instead, we calculate the mass fraction

$$f = \mathcal{M}_B / (\mathcal{M}_A + \mathcal{M}_B) = \alpha_A / (\alpha_A + \alpha_B) = \alpha_A / a, \quad (9)$$

where  $\alpha_B = a - \alpha_A$ . This parameter,  $f$ , also given in Table 10, creates a ratio of the two quantities directly obtained from the observations: the vA 351A semi-major axis ( $\alpha_A$  from POS mode, Figure 8) and the relative orbit size ( $a$  from TRANS mode, Figure 1), listed in Table 10. From these we derive a mass fraction of  $0.443 \pm 0.022$ . Equations 5, 6, and 7 yield  $\mathcal{M}_A = 1.14 \pm 0.14 \mathcal{M}_\odot$  and  $\mathcal{M}_B = 0.91 \pm 0.11 \mathcal{M}_\odot$ .

The mass errors of  $\sim 12\%$  exceed any of our past (Benedict et al. 2016; Benedict et al. 2001) determinations. We ascribe this to a combination of orbit low inclination and high eccentricity, increasing the errors on relative orbit size and perturbation size, and primarily to the parallax error on what is the smallest parallax yet measured for a binary by the *FGS*. The median parallax in our previous MLR work was 113 mas, 6 times larger than that measured for vA 351. The median percent error in our MLR study was 0.4%, significantly better than the vA 351 3.5% parallax error.

Nonetheless, vA 351B with  $\mathcal{M}_B = 0.91 \mathcal{M}_\odot$  is consistent with a G5V star, and vA 351A with  $\mathcal{M}_A = 1.14 \mathcal{M}_\odot$  an F8V star (Cox 2000). This is not consistent with each component being a single low mass red dwarf as suggested by the Figure 5 color-color diagram, which cleanly and unambiguously identifies vA 351 as such. To make up for the excess mass we now identify component A to have a companion, component D. Component B also must have a companion, component C. We now assert that  $\mathcal{M}_A + \mathcal{M}_D = 1.14 \mathcal{M}_\odot$  and  $\mathcal{M}_B + \mathcal{M}_C = 0.91 \mathcal{M}_\odot$ .

## 5. PHOTOMETRY

### 5.1. *FGS* POS Mode Photometry

*FGS3* has demonstrated relative photometric precision approaching the milli-magnitude level for two other M

dwarf stars, Proxima Cen and Barnard’s Star (Benedict *et al.* 1998). The *FGS* acquires data at a 40Hz rate with each observation lasting from 80 to 130 seconds. With similar exposures and a brightness two magnitudes fainter than Proxima Cen, measures of vA 351 have lower S/N. We flat-fielded the vA 351 observations using a sum of the average counts for astrometric reference stars ref-2 and ref-3 identified in Figure 4. Figure 9 contains flat-fielded average counts as a function of BC orbital phase. We observed vA 351 three times during each scheduled *HST* observation set, hence, the vA 351 groupings of three. The observations used the *FGS3* F583W filter. The bandpass center, 583nm, has a width 234nm, which includes both the H $\alpha$  and HeI emission lines discussed below (Section 7). Figure 9 includes a sine wave with a period constrained to the BC orbital period. We find a F543W ( $V+H\alpha$ ) amplitude of  $0.021\pm 0.005$  mag. The sampling is too sparse to make definitive statements, but the fit to the BC orbital period indicates only one dimming event per cycle, when vA 351B is more distant than vA 351C. This might require additional complications (such as eclipses or a dark spot on the back side of component C). Alternatively, because vA 351 varies ( $V^*$  V805 Tau, flare star), we might attribute the larger signal at  $\Phi_{BC} \simeq 1$  to flaring activity.

### 5.2. *V*-band Photometry

To test the eclipse hypothesis, one of us (BS) obtained absolute *V*-band photometry in autumn 2019 using the Lowell Observatory 0.7-m robotic telescope. vA 351 was observed with 100-second exposures, typically several visits each on a total of 13 nights, using “Canopus” software<sup>2</sup> to reduce the data, yielding conventional aperture photometry. The zero-point was adjusted to within a few percent of standard *V* using magnitudes of four field comparison stars.

Rather than providing additional evidence to assist in choosing between the interpretations above (Section 5.1), a periodogram analysis of the newer *V*-band photometry yields a highly significant peak near,  $P_V = 1.7^d$  with a lower peak near the BC orbital period,  $P_{BC} = 0.7^d$ . Fitting a sine curve to the *V* photometry yielded  $P_V = 1.783 \pm 0.003^d$  and an amplitude  $\Delta V = 0.011 \pm 0.001$  magnitude with  $\langle V \rangle = 13.27$ .

The left side of Figure 10 presents the *V* measurements phased to the  $1.783^d$  period with the *FGS* F543W measurements superposed. The fit includes only the Lowell *V* measurements, The right side of Figure 10 phases *FGS* and *V* photometry to the BC orbital period with the single cycle fit from Figure 9 superposed. The variation in *V* only does not correlate with the vA 351 BC orbit. The bandpass containing H $\alpha$  does.

### 6. DISSECTING vA 351

Our astrometry (Section 4.6) yields masses for the component A,D and the component B,C pairs. Our RV measurements (Section 3.4) yield a mass ratio for the B,C components. From  $M_{BC}=0.91 \pm 0.11M_\odot$  and  $M_C/M_B=0.945\pm 0.005$  we find  $M_B=0.47\pm 0.06M_\odot$  and  $M_C=0.44 \pm 0.06M_\odot$ . Assuming for the AD-BC pair a  $\Delta K = 0$ , that  $K_B \simeq K_C$ ,  $A_K \simeq 0$ , and from our parallax, a distance modulus  $m-M=3.68$ , we find absolute

magnitudes  $M_K = 6.09$  for each. The Benedict *et al.* (2016) *K*-band MLR predicts  $\mathcal{M}=0.46M_\odot$ , assuming equal brightness components B and C. The agreement provides validation for the astrometry and RV results. We now lack only individual masses for components A and D.

To establish their masses we use the data and sources listed at the top of Table 11. This table also provides a line by line guide to the process resulting in a mass estimate for components A and component D, the (suspected) white dwarf required to satisfy the total mass resulting from the astrometry (Section 4.6).

Table 11 begins with photometry of the total system, *V*-band from Section 5.2 and *K*-band from 2MASS (Skrutskie *et al.* 2006) on **line 1**. We transform these into arbitrary intensities (**line 2**), and assert a magnitude difference between components AD and BC on **line 3**. In support of the **line 3** data, Table 1 contains magnitude differences in various bandpasses. The *FGS* TRANS F583 measures are close to *V*-band (Henry *et al.* 1999). The speckle magnitudes are similar to *r* and *i* (Horch *et al.* 2012). Some of the components of vA 351 are quite active, but, without the flare events on mJD 50481 and 56934, the measures are consistent with  $\Delta V = 0.0 \pm 0.1$ . Typically  $\Delta K$  is less than  $\Delta V$  for M dwarfs (Benedict *et al.* 2016), supporting an estimate of  $\Delta K = 0.0 \pm 0.03$ . Finally we introduce (**line 4**) estimates of interstellar absorption, taking as priors a little less than half the total absorption of  $A_V = 1.17$  mag (with  $A_K/A_V = 0.11$ ) along this line of sight (Schlafly & Finkbeiner 2011). Including an absorption parameter significantly reduced the Table 11 solution residuals, and brought the *V* and *K* results into closer agreement.

Next we introduce (**line 5**) data provided by the RV measures, the  $M_C/M_B$  mass ratio from the absorption line results (Figure 2, Table 6),  $M_C/M_B = 0.945\pm 0.005$ . **Lines 6-10** introduce the mass and parallax data from the astrometric modeling results (Table 10).

We then appeal to three external relationships, allowing us to estimate a mass from an absolute magnitude. The first two relate M dwarf intrinsic luminosity to mass. Rather than use the fifth-order polynomial Luminosity to Mass relations (LMR) in Benedict *et al.* (2016), we simplify to a linear LMR for the *V*-band and a parabolic LMR for the *K*-band,

$$\mathcal{M} = C_0 + C_1(M_{V,K}) + C_2(M_K)^2 \quad (10)$$

with coefficients given in Table 12. The total dynamical mass of vA 351 precludes very low component masses, where the considerable non-linearity in the LMR requires higher order terms. The third relation maps *K*-band absolute magnitude as a function of mass for white dwarf stars. We obtain this mapping from Bergeron cooling models (Holberg & Bergeron 2006; Kowalski & Saumon 2006; Tremblay *et al.* 2011; Bergeron *et al.* 2011), assuming a Hyades age of 670 My (Gossage *et al.* 2018). Figure 11 shows this mapping, and a relation fit with a third order polynomial with offset,

$$\mathcal{M} = C_0 + C_1(M_K - X_0) + C_2(M_K - X_0)^2 + C_3(M_K - X_0)^3 \quad (11)$$

with the coefficient zero-point at the bottom of Table 12. Figure 11 shows a multi-valued relation between mass and luminosity (in a very narrow luminosity range) for

<sup>2</sup> <http://bdwpublishing.com/mpocanopusv10.aspx>

the  $V$ -band. Hence, in the least-squares analysis below we only use the  $K$ -band to determine the WD mass.

We next search for component intensity values, system parallax, and line of sight absorption (**lines 11-16**) that minimize the sum of the squares of the O-C residuals, where O are the **line 1-10** values, and C are the **line 17-24** final parameter values and residuals for both  $V$  and  $K$  bandpasses. We transform the **line 11-14** intensities into the **line 26 - 30** magnitudes (corrected for the estimated absorption) and then with the parallax (yielding a distance modulus,  $m-M = 3.68$ ) into the **line 31 - 35** absolute magnitudes. Using Equations 10 and 11 we derive the **line 36 - 39** masses. This sequence iterates (separately for both the  $V$ - and  $K$ -bands) until minima in the sums of the squares of the **line 17 - 24** residuals are found (**line 25**). The  $K$ -band yields a significantly better fit with smaller residuals.

We find final masses by applying the above least-squares process to both the  $V$ - and  $K$ -band data, then averaging the results (**lines 36-40**). We find  $\mathcal{M}_A = 0.53 \pm 0.10 M_\odot$ ,  $\mathcal{M}_B = 0.43 \pm 0.04 M_\odot$ ,  $\mathcal{M}_C = 0.41 \pm 0.04 M_\odot$ , and  $\mathcal{M}_D = 0.54 \pm 0.04 M_\odot$ , where the errors are from the intrinsic scatter in the  $V$ - and  $K$ -band MLR. The WD mass,  $\mathcal{M}_D$ , comes only from the  $K$ -band photometry. The major mass disagreement between the  $V$ - and  $K$ -band is for component A. None of these M dwarf masses can contribute new data points for the Benedict et al. (2016) MLR, having been derived by appeal to that MLR.

The **line 25** fit quality parameter is much worse for the  $V$ -band. We find those values are decreased to 1.31 for  $V$  and 0.001 for  $K$  by including a larger absorption prior,  $A_V = 0.59$ ,  $A_K = 0.05$ . This change also improves the A,B,C component mass agreement, yielding  $\mathcal{M}_A = 0.56 \pm 0.07 M_\odot$ ,  $\mathcal{M}_B = 0.46 \pm 0.01 M_\odot$ ,  $\mathcal{M}_C = 0.44 \pm 0.01 M_\odot$ , and  $\mathcal{M}_D = 0.53 \pm 0.04 M_\odot$ . However, Taylor (2006) concludes that Hyades interstellar extinction is negligible. Thus, if real, this extinction must be local to vA 351. However, photometry with the Wide-field Infrared Survey Explorer (WISE) (Wright et al. 2010) shows no excess far-IR flux indicating heated dust that might increase local absorption. We note that the Table 11 WD  $V - K = +1.18$  far exceeds that predicted for a 670My old  $0.54 M_\odot$  WD,  $V - K = +0.3$ . The fit including a higher absorption yields the same WD mass, but a  $V - K = +0.66$  much nearer to that predicted.

We estimate the WD mass error from the scatter in the Figure 11 LMR, and have ignored any contributions from the WD and Hyades age uncertainties. The inputs to our mass derivation (**lines 1 - 10**) provide very little leverage with which to assign an age to the WD. For example, our assumed WD age of 670My and a mass,  $\mathcal{M}_D = 0.53 M_\odot$ , yields from the Bergeron cooling models an absolute magnitude  $M_K = 12.01$ . An age of 400My for that same mass WD yields  $M_K = 11.75$ . However the other components have  $M_K \sim 6$ , over  $100\times$  brighter, rendering the WD component age ineffective at changing the mass results (**lines 36 - 40**).

The IGRINS spectra yielded an AD-BC  $\Delta H = 0.28 \pm 0.10$ . Relatively normal M dwarf binary stars would evidence  $\Delta K \simeq \Delta H$ . Redoing the modeling outlined in Table 11, substituting in **line 3**  $\Delta K = 0.28 \pm 0.1$  for  $\Delta K = 0.0 \pm 0.03$  yields slightly higher masses for com-

ponents B, C, and D (each up by  $0.02 M_\odot$ ), and a slightly lower mass for component A (down by  $0.04 M_\odot$ ). However the  $K$ -band goodness of fit parameter (**line 25**) increases by a factor of 20. Thus, a lower  $\Delta K$  value is a better fit to our aggregate information.

From the Table 11 component B and C masses and the RV amplitudes,  $K_A$  and  $K_B$  from Table 6, we can derive an inclination of  $i_{BC} \simeq 23^\circ$  and a separation,  $a_{BC} \simeq 0.016$  AU. Estimating component radii using the Boyajian et al. (2012) eclipsing binary mass-radius relation, components B and C are separated by  $\sim 4$  stellar diameters. Furthermore, if we assume that B and C are synchronized in the 0.75-day orbit, and spin-orbit aligned, as it seems very likely, we can predict a  $30 \text{ km s}^{-1}$  equatorial rotational velocity for a typical radius of  $0.46 R_\odot$  for a  $0.46 M_\odot$  star (Boyajian et al. 2012). Our analysis of the CfA and IGRINS spectra (Section 3.4) yielded  $v \sin i \simeq 11 \text{ km s}^{-1}$ , implying  $i_{BC} \simeq 20^\circ$ .

We have established that the vA 351 system contains four components with components A and D orbiting a common center of mass and components B and C orbiting a common center of mass. The AD subsystem and BC subsystem orbit a common center of mass. Radial velocity measurements easily detect and characterize the BC motion (Figure 2) and the AD-BC orbit (Figure 3). The residuals to the BC RVs cannot contain any signature of the AD RVs. However RV measures of component A might evidence AD motion. Additionally, when measured by FGS TRANS and speckle the separation between A and the BC subsystem should change because of the AD motion. Component A dominates the TRANS fringe for AD, because A is  $> 3$  magnitudes brighter than component D. Component A will thus be measured to be nearer to or more distant from BC because it orbits a barycenter with a WD, component D.

In an attempt to tease out possible effects of component D on component A we appeal to periodograms. Figure 12 presents Lomb-Scargle periodograms for (top) the time series of x and y TRANS residuals to the relative orbit shown in Figure 8, and (bottom) for the time series of residuals to the component A RV orbit (Figure 3). We find one significant peak in the component A RV power spectrum at  $P = 21^d$  with a false alarm probability  $< 0.1\%$ . As expected, the Figure 2 B and C RV residuals have no significant power in the range  $500^d > P > 8^d$ . The TRANS X and Y residuals contain a peak produced by a slight increase of power in both axes at  $P \sim 25^d$  with a false alarm probability  $> 50\%$ . That the only peak simultaneously present in both the TRANS astrometric residuals and the component A RV occurs at near  $P \sim 21^d$  suggests an AD period near that value.

A formal fit of a sine wave to the RV A residuals yields  $P_{AD} = 20.82 \pm 0.01^d$ , and  $K_A = 0.30 \pm 0.09 \text{ km s}^{-1}$ . Our  $\mathcal{M}_A$ ,  $\mathcal{M}_D$ , and a circular orbit with this period yield a vA 351A perturbation of 1.5 mas, a total separation,  $a_{AD} \simeq 0.15$  AU, and would require a nearly face-on orientation,  $i_{AD} > 89^\circ$ , to produce the small RV amplitude detected. Additional evidence for this orientation includes the near zero vA 351A  $V \sin i$  (Section 3.4).

## 7. EMISSION LINES

### 7.1. $H\alpha$

Early in our spectroscopic data collection process it became apparent that vA 351 exhibited a strong and quite variable H $\alpha$  emission with between one and four components. Given that we obtained the many observations under a large range of weather conditions, any inter-comparisons of H $\alpha$  behavior are best carried out using normalized data. We transformed all H $\alpha$  data to normalized counts, allowing the determination of equivalent width (hereafter, EW).

To measure EW we transformed the intensities,  $I(\lambda)$  thusly;

$$AW = (1 - (I(\lambda)/(I(\lambda)))) \quad (12)$$

where  $\langle I(\lambda) \rangle$  averages two ranges, I(6547Å-6556Å) and I(6572Å-6584Å). To ensure high enough S/N for inclusion in subsequent analysis, the measured background,  $\langle I(\lambda) \rangle$ , had to exceed 40 counts per pixel (S/N $\sim$  9). We used a Gaussian multi-peak fitting routine in the GUI-based commercial package *IGOR*<sup>3</sup> to derive component wavelength (for some RV determinations we used a Voigt function) and EW from a 6Å span centered on the H $\alpha$  region of each spectrum. Component FWHM typically ranged from  $0.3 < \text{FWHM} < 0.7\text{Å}$ . Figure 13 provides an example of the fitting process. We tabulate the resulting H $\alpha$  EW in Å in Table 13 with component 1,4 (vA 351C and B, see below) velocities in Table 14 and component 2,3 velocities in Table 15. While the average total H $\alpha$  EW,  $\langle \text{EW}_{\text{tot}} \rangle = -6.9 \pm 1.0$ , indicates a highly active *single* star (Newton *et al.* 2017), vA 351 is not a single star. The individual EW for components B and C ( $\langle \text{EW}_B \rangle = -1.1 \pm 0.2$ ,  $\langle \text{EW}_C \rangle = -0.9 \pm 0.3$ ), when placed on the Newton *et al.* (2017) figure 2, argue only slight component over active for their masses. Alonso-Floriano *et al.* (2015) find an  $\text{EW}_{\text{tot}} = -7.0$  on mJD=55935, consistent with our measures in the range  $49962 < \text{mJD} < 54484$ .

We probed H $\alpha$  velocity behavior close to syzygy (phases  $\Phi_{BC} = 0.25$  and  $0.75$ ) on those nights we were able to obtain observations closer to quadrature ( $\Phi_{BC} = 0$  and  $0.5$ ). We constrained peak parameters (amplitude, width, and Voigt shape) to near quadrature values, solving only for position in wavelength, as demonstrated in Figure 14. This approach depends on an assumption of profile stability for EW2, EW3 over hours, and provides no independent EW information at syzygy for any component.

When we first observed four components in H $\alpha$ , these were ascribed to components A, B, C, and now D (3, 4, 1, and 2 in Figure 13). B and C were easily identifiable with peaks 4 and 1, given their known, short-period RV behavior from absorption lines (Figure 2). Figure 16 shows component B and C RVs from H $\alpha$  emission as a function of BC absorption line orbital phase. Table 6 includes the results of orbit fitting to all resulting component B and C H $\alpha$  RVs. The  $K_B$  and  $K_C$  amplitudes from H $\alpha$  significantly exceed those derived from the absorption lines. The strikingly systematic residuals seen in Figure 16 might be explained by some sort of flow pattern. For example the component B positive residuals in the ranges  $0.1 < \Phi < 0.25$  and  $0.75 < \Phi < 0.9$  indicate outflow from component B. This flips to negative RV residuals

towards component B (inflow) for  $0.25 < \Phi < 0.35$  and  $0.75 < \Phi < 0.9$ . The residuals for component C invert this sequence, indicating that a similar process works on both stars.

The bottom panel of Figure 17 plots H $\alpha$  EW values for components B and C, which show strong correlation with BC orbital phase. The top of Figure 17 demonstrates that the sum of EW2 and EW3 show no such correlation, arguing that these components have little association with vA 351B and C. Returning to the lower panel, EW B is slightly larger than EW C at quadrature phase  $\Phi_{BC} = 1.0$  or  $0.0$ . EW C is significantly larger than EW B at the quadrature phase  $\Phi_{BC} = 0.5$ . These observations are consistent with the leading hemispheres of both stars having increased H $\alpha$  activity, component C more so than B. In general component B and C H $\alpha$  EW is highest near quadrature ( $\Phi_{BC} = 0.0, 0.5, 1.0$ ), consistent with the wide-band photometry (Figure 9), showing a brighter total magnitude near those phases. With an estimated  $20^\circ$  inclination, apparently the H $\alpha$  emission suffers attenuation at syzygy ( $\Phi_{BC} = 0.25, 0.75$ ). While we have no direct H $\alpha$  EW measures for vA 351B and C at syzygy, the patterns in Figure 17 show a reduction in EW as either component approaches syzygy, supporting that hypothesis.

The period derived from the H $\alpha$  B and C components agrees with that from absorption lines (Figure 2). The far larger  $K_B$  and  $K_C$  amplitudes do not agree. We offer a working hypothesis to explain this inconsistency. H $\alpha$  becomes excited at some point between components B and C (labeled 4 and 1 in Figure 13). If a ring or cloud exists around each star, the hydrogen gas gets excited between the two components, then diffuses around to the opposite side, where shadowing cools the gas, allowing the hydrogen to emit H $\alpha$ . To produce the larger  $K_B$  and  $K_C$  amplitudes requires cloud/ring radii approximately  $1.7\times$  the star radius. Location in each shadow increases the distance between gas and barycenter. Exhibiting a similar period, the emitting gas travels further in the same time, meaning it has a higher velocity.

We provide an animation (Figure 15, *HalpawEBbetter.mp4*) illustrating the behavior of the various components of the H $\alpha$  emission as a function of B-C orbital phase. We construct the animation using only results of the constrained probing exemplified by Figure 14. The traces have been shifted in wavelength to minimize component 2 position changes (Figure 13) from frame to frame. Originally produced to highlight the RV behavior of components B and C (4 and 1 in Figure 13), the animation also shows the positional (RV) and EW constancy of components 2 and 3. For the 129 values in Table 15 peaks 2 and 3 have  $\Delta \text{RV} = 35.4 \pm 3.4 \text{ km s}^{-1}$  and for the 140 values in Table 13, a  $\Delta \text{EW} = 0.02 \pm 0.29$ . This consistency argues for their having the same source, presumably associated with either vA 351A and/or D. Figure 18, showing the average of component 2 and 3 RVs plotted against the AD-BC orbital period phase,  $\Phi_{AD-BC}$ , lends support to this assertion. The RVs exhibit significant scatter, but agree with the orbit derived from the Figure 2 absorption-line orbit. The bifurcation of the central H $\alpha$  component (labeled 2 and 3 in Figure 13) could be either self-absorption (e.g. Semaan *et al.* 2013; Pavlenko *et al.* 2019) in a rotating cloud or emission from a rotating ring, either associated

<sup>3</sup> <https://www.wavemetrics.com>



with A, or D, or both.

In Section 6 we provided evidence for a roughly 21<sup>d</sup> periodicity associated with vA 351A RV residuals to the AD-BC orbit, presumably because of the orbit of vA 351A around the AD barycenter. Figure 18 identifies H $\alpha$  components V2 and V3 with the AD pair. The periodograms of V2 and V3 in Figure 19 solidify that association, showing a very strong signal,  $P \sim 25^d$  in the sum of the individual periodograms. Fitting sine waves to the V2 and V3 RVs yield  $P_{V2} = 25.6 \pm 0.1^d$ ,  $K_{V2} = 2.3 \pm 0.4$  km s<sup>-1</sup>,  $P_{V3} = 25.8 \pm 0.1^d$ , and  $K_{V3} = 1.4 \pm 0.4$  km s<sup>-1</sup>. Again, if a consequence of the A-D orbit, the low  $K$  values suggest a nearly face-on orbit.

### 7.2. He I

In the CE spectra the  $\lambda$  5876.6Å He I line appears in emission with from one to three components. This line typically appears in stellar absorption spectra in B and hotter stars, requiring  $T > 10,000\text{K}$  (Cox 2000). Re-inspection of CE M dwarf spectra acquired in support of our MLR project (Benedict et al. 2016) shows the He I line in emission for systems with primary mass less than  $0.27\mathcal{M}_{\odot}$  (G1234, G1791.2, G1473, G165) and absent for systems with primary mass  $\mathcal{M} \geq 0.33\mathcal{M}_{\odot}$  (G122, G1469, G1623, G1831, GJ1081, G250-029). Thus, it is surprising that vA 351B and C, with  $\mathcal{M} \simeq 0.50\mathcal{M}_{\odot}$ , show He I emission.

Figure 20 contains a plot of  $AW$  (Equation 12, with background local to the He I line) as a function of wavelength for some of the higher S/N observations (same epochs of observation as for Figure 13). We produced He I EW and RVs (as for H $\alpha$ ), listed in Table 16 and Table 17 and plotted in Figure 21 (RVs) and Figure 22 (EW). We label the central He I component EW2 and  $V_{\text{cen}}$ . Our He I EW and RV measures contain significantly more noise than for H $\alpha$ .

Again, the RV behavior (Figure 21) of the higher and lower velocity peaks identify them as coming from components B and C. The lower S/N precludes probing in closer to syzygy as we did for H $\alpha$  (Figure 14). However, unlike H $\alpha$ , the component B and C RVs from He I more closely track the absorption line results, yielding similar  $K_B$  and  $K_C$  RV amplitudes, with results listed in Table 6. This argues that excitation and re-emission of He I occurs closer to each stellar surface. Residuals indicate that, as for H $\alpha$ , simple, zero eccentricity orbital motion is an inadequate model for the motions of the He I emission. We ascribe EW2 and  $V_{\text{cen}}$  to the vA 351 AD components (see below for rationale). We derive He I EW averages from the Table 16 values:  $\langle \text{EW}_B \rangle = -0.29 \pm 0.12$ ,  $\langle \text{EW}_C \rangle = -0.34 \pm 0.14$ ,  $\langle \text{EW}_{\text{cen}} \rangle = -0.64 \pm 0.45$ ,  $\langle \text{EW}_{\text{tot}} \rangle = -1.17 \pm 0.48$ . Similar to H $\alpha$ , most of the He I emission comes from the central source presumably associated with components A and D.

Figure 23 shows the Table 17  $V_{\text{cen}}$  RVs plotted against the AD-BC orbital phase with the absorption line RV orbit overplotted. While quite noisy, the  $V_{\text{cen}}$  velocities argue for the association of the central He I emission with the AD components of vA 351.

An initial supposition, that proximity heating (components B and C separated by only 0.016 AU) excites both H $\alpha$  and He I emission can easily be falsified. Our Sun with  $T_{\text{eff}} = 5777\text{K}$  has a surface emissivity  $F_{\odot} = 6.32 \times 10^{10}$  erg cm<sup>-2</sup>s<sup>-1</sup> (Cox 2000). With

masses near  $0.5\mathcal{M}_{\odot}$  (Table 11, lines 35-36), components B and C would have  $T_{\text{eff}} \simeq 3800\text{K}$  (Cox 2000) and  $F_{\odot} = 1.18 \times 10^{10}$  erg cm<sup>-2</sup>s<sup>-1</sup>, assuming  $F \propto T^4$ . For a separation  $r=0.016$  AU (Section 6) the energy received by either component from the other is insufficient to raise the surface temperature to the 10000K necessary to excite the He I emission. This excitation level requires a non-thermal source, perhaps a flare-induced mechanism (Kowalski & Allred 2018) or magnetic fields.

Relative to the latter, Donati et al. (2008) and Morin et al. (2008, 2010) have mapped the magnetic fields of a set of M dwarf stars. They find that most M dwarfs have poloidal fields which increase in intensity with rotation rate. Presuming tidal locking for components B and C, their sub- one day rotation period and  $0.5\mathcal{M}_{\odot}$  masses would suggest a magnetic field for each of  $\sim 500$  Gauss (e.g. Morin et al. 2011, figure 2). Perhaps an interaction of the component B and C magnetic fields excites the H $\alpha$  and He I emission. Additionally, component poloidal fields might serve to focus energy to polar locations, similar to terrestrial aurorae. We have no concrete evidence that the He I emission arises near there. Alternatively, perhaps the magnetic field is a mix of poloidal and toroidal, with He I emission scattered near the stellar surface. Table 16 has time-resolved data with which to tease out more hints as to excitation and emission. Doing so is beyond the scope of this paper. We hope that our observational data will stimulate the derivation of details of some magnetohydrodynamic mechanism operating in this system.

Lastly, we explore some relations between the various emission line EW. Figure 24, left, shows the strong correlation between H $\alpha$  component 2 and 3 EW from Table 13. We plot the log of the absolute value of EW2,  $\log|\text{EW}2|$ , against  $\log|\text{EW}3|$ . The maximum values in the upper right all occur within 4 days of AD-BC periastron. We have weaker evidence that the same energy source(s) power both the H $\alpha$  and He I emission associated with vA 351 AD, shown by their correlation (Figure 24, right). The one strongest He I point also occurred near AD-BC periastron.

### 7.3. X-ray Emission

D'Elia et al. (2013) catalog transient 0.3-10keV X-ray bursts observed by Swift-XRT (Gehrels et al. 2004). During the seven years of operation documented in the catalog, vA 351 was detected three times, listed in Table 18. We tag each observation with both the BC and AD-BC orbital phases. In a 5 $^{\circ}$ -radius subset of the catalog centered on vA 351, it is among the brightest with an average 0.3-10keV flux,  $\langle \text{Flux} \rangle = 1.62 \times 10^{-12}$  mW m<sup>-2</sup>. Two detections occurred close to BC syzygy, phase  $\Phi_{\text{BC}} \sim 0.25, 0.75$ . One detection occurred very close to AD-BC periastron. The BC syzygy correlation suggests the presence of active (coronal?) regions on the side of each star facing the other (i.e., facing the observer at syzygy), perhaps associated with dark spots. The BC system is fainter at phase  $\Phi_{\text{BC}} = 0.75$  (Section 5.1, Figure 9), when vA 351B is closest to us. Dark spots on the hemispheres of each star facing the other might explain both features. From admittedly small number statistics we abstract that some X-ray behavior comes from BC, some from periastron interaction of AD with BC.

## 8. DISCUSSION

With all of these (sometimes conflicting) results we now search for a coherent description of the entire vA 351 system. To do so, we summarize measured results, identify inferences drawn from these results, clearly label conjectures, and end with constructing a provisional picture of vA 351.

*FGS* TRANS mode and speckle camera astrometry confirm vA 351 binarity with a high eccentricity, low inclination orbit, producing a total mass requiring more than just two M dwarfs. TRANS and speckle measures provide a near-zero magnitude difference between the the originally identified components A and B. RVs acquired from two primary sources yield a component A-B orbit agreeing with the TRANS/speckle result. These RVs also identify two M dwarfs in a very short period, circular orbit,  $P_{BC} = 0.749^d$ . CfA and IGRINS analyses yield  $v \sin i \simeq 11 \text{ km s}^{-1}$  for each component. The  $K$  values for vA 351B and C provide  $\mathcal{M}_C/\mathcal{M}_B=0.945$ . *FGS* POS mode astrometry yields an independent parallax, a proper motion, and a mass fraction,  $f$ . The mass fraction shows  $\mathcal{M}_A$  far too large to be only an M dwarf. To component A we add component D, presumed to be a white dwarf.  $\mathcal{M}_B$ , too large to be a single M dwarf, now acquires component C, known from RV spectra to be another M dwarf. We derive individual masses for all components, using the distance, total masses, masses of detected components, AD-BC magnitude difference, an estimate of interstellar extinction,  $\mathcal{M}_C/\mathcal{M}_B$  mass ratio,  $V$ - and  $K$ -band Mass-Luminosity relations, and a  $K$ -band WD Mass-Luminosity relation (assuming a 670 My age for the Hyades).

The values for  $\mathcal{M}_B$  and  $\mathcal{M}_C$  and the observed RV amplitudes yield an orbital inclination,  $i_{BC} \simeq 25^\circ$  and a physical separation,  $a_{BC} \simeq 0.016 \text{ AU}$ . This inclination is consistent with an observed  $v \sin i \simeq 11 \text{ km s}^{-1}$ , plausible B and C radii, spin-orbit alignment, and tidal locking. Periodograms of vA 351A absorption line RVs and variations in AD-BC separation suggest  $P_{AD} \sim 22^d$ .  $\mathcal{M}_A$ ,  $\mathcal{M}_D$  and a presumed astrometric detection limit yield an orbital inclination,  $i_{AD} \simeq 90^\circ$ , and for a circular orbit, a physical separation,  $a_{AD} \sim 0.2 \text{ AU}$ .

We observe  $H\alpha$  in emission with from two to four components. Components B and C are easily identified through RV variation with the same period,  $P_{BC} = 0.749^d$ . These variations have larger velocity amplitudes than for the absorption lines. The  $H\alpha$  BC velocity variation with larger amplitude than seen for the absorption line measures likely places the  $H\alpha$  emission further from the BC system barycenter, behind, in the shadow of each component, where it can cool sufficiently to emit. The EW behavior, phased to the BC orbital period and residual patterns seen for the  $H\alpha$  RV BC orbits offers supporting evidence. The two central  $H\alpha$  peaks have an RV signature agreeing with that for component AD-BC orbit. Periodograms of their RVs show a strong peak at  $P \sim 25^d$ .

We observe HeI in emission at  $\lambda 5875\text{\AA}$  with from one to three components. Again, identification of components B and C come from RV variation with the same period,  $P_{BC} = 0.749^d$ , this time with velocity amplitudes similar to those from absorption lines. This suggests closer proximity of the HeI emission regions to

each component B and C. We ascribe B, C emission, which requires an excitation temperature,  $T \sim 10,000\text{K}$ , to non-thermal heating effects, either near continuous micro-flaring or magnetic field interactions. The RVs of the strongest HeI peak identifies it with either A and/or D.

X-ray emission has been detected when B-C are near syzygy, phase  $\Phi_{BC} \sim 0.25, 0.75$ . One outburst occurred very near AD-BC periastron. Based on sparse sampling, *FGS* photometry (with an F583W bandpass containing  $H\alpha$ ) suggests that the system is fainter at B-C orbital syzygy, B nearer to us than C. Spots on each hemisphere of components B and C facing the other could satisfy the photometry. Spots associated with stellar activity could then explain the X-ray coincidence with BC syzygy. A remaining photometric mystery is that the  $V$ -band photometry yields  $P_V = 1.78^d$ , a variation unidentifiable with any previously determined activity.

When initially formed, all components of vA 351 could have had radii significantly larger than at present. For example the  $0.4\mathcal{M}_\odot$  components of PAR 1802 in the Orion Nebula Cluster (age 1 My), have radii  $R \simeq 1.65R_\odot$  (Gómez Maqueo Chew *et al.* 2012), four times larger than drawn in Figure 25. This raises the interesting possibility that the AD and BC separations have changed over time. Naoz & Fabrycky (2014) and Naoz (2016) demonstrate that the Kozai-Lidov Effect could force BC into a smaller separation, effected by interactions with the more distant AD components, which might be treated as a single mass. On the other hand  $\mathcal{M}_{BC}$  acting as a single mass could have rearranged components A and D into a smaller separation orbit. This latter orbital evolution almost certainly had to occur, given that the WD component D, if similar to other known WD Hyads, had a  $\sim 3\mathcal{M}_\odot$  (Salaris & Bedin 2018) early A to late B progenitor, whose red giant phase would have engulfed component A at the inferred, present A-D separation.

## 9. CONCLUSIONS

These results support a final picture: a binary subsystem with M dwarf component A and white dwarf component D with  $P_{AD} \sim 22^d$  lies 0.5-4.4 AU from a binary subsystem with components B and C, both M dwarf stars. The AD-BC inclination,  $i_{AD-BC} = 14^\circ \pm 8^\circ$ , compared to our inferred B-C inclination,  $i_{BC} \sim 20^\circ$  suggests coplanarity.

The cartoon in Figure 25 shows the B and C components of the total system as seen from Earth, with an inclination inferred from the derived masses (Table 11) and absorption line  $K_B$  and  $K_C$ , with parallax (Table 9) impressing a scale in AU. In the absence of any measure, we have constrained the position angle of the line of nodes,  $\Omega$ , to that of the AD-BC orbit. We take the component stellar sizes from the Boyajian *et al.* (2012) mass-radius relation for eclipsing binaries, they typically having short orbital periods, as does vA 351 BC. The  $H\alpha$   $EW_{B,C}$  trend towards smaller values as  $\Phi_{BC}$  approaches 0.25 or 0.75 in Figure 17, demonstrating some eclipse (or darker spot) behavior in whatever excites the  $H\alpha$  emission. Seen from the other one, both the B and C components subtend only  $20^\circ$  on the sky.

It is difficult to choose among accretion, stellar winds, continuous microflaring, and magnetic field interactions to stimulate the  $H\alpha$  and HeI emission lines. We illus-

trate our hypothesis in Figure 25. The H $\alpha$  emission, once excited anywhere, can sufficiently cool enough to emit H $\alpha$  in shadowed regions near the triangles (always close to components B and C, respectively), at the distance from the BC system center of mass required to produce the observed H $\alpha$  RV  $K$  values. We estimate their placement by solving Equation 7 for  $\alpha$  values constrained by our now known parallax and period, and the higher H $\alpha$   $K$  values (Figure 16, Table 6). The fat arrows in Figure 25 indicate notional coronal loop-like flows or circulation that we infer from the H $\alpha$  RV residuals in Figure 16. We have made no attempt to provide detailed flow patterns. The HeI emission (from EW, Figure 22) varies little and its velocity matches that from absorption lines, so is likely produced near the stellar surface. The HeI RV residuals in Figure 21 hint at a flow pattern similar to that of H $\alpha$ . These data do not constrain an exact HeI excitation location (other than near the stellar surfaces), but observations of active M stars would suggest the polar regions of each component. We offer no hypothesis explaining the genesis of H $\alpha$  and HeI emission associated with the AD pair, other than to point out that a 670 My old,  $0.53M_{\odot}$  WD would have a surface temperature capable of producing such emission.

#### 10. SUMMARY

1. Fringe scans (TRANS mode) spanning 4.7 years and a few more recent speckle observations yield a low inclination, highly eccentric orbit. They also provide component  $\Delta V$  measurements, indicating nearly equal brightness components.
2. Absorption-line radial velocities from the McDonald Observatory 2.1m telescope and Cassegrain Echelle spectrograph and a long series of observations from the CfA Digital Speedometer yield an RV orbit which agrees with that derived from astrometry. They also yield a period and mass ratio for two, short orbital period M dwarf components (now identified as B and C) of this system, with  $P_{BC} = 0.7492425 \pm 0.0000003$  days.
3. Spanning 1.8 years, fringe tracking (POS) observations of vA 351A, including photocenter corrections, provide an absolute parallax with a 4% error,  $\varpi_{\text{abs}} = 18.37 \pm 0.65$  mas, a proper motion, and a mass fraction relative to the astrometric reference frame. This parallax establishes Hyades membership for vA 351, satisfying our first goal.
4. The astrometric solution yields period,  $P = 2.705 \pm 0.004$  y, and a total mass for the system,  $\mathcal{M}_{\text{tot}} = 2.06 \pm 0.24M_{\odot}$ . The mass fraction provides  $\mathcal{M}_A = 1.14 \pm 0.14M_{\odot}$  and  $\mathcal{M}_B = 0.91 \pm 0.11M_{\odot}$ , masses inconsistent with M dwarf components. We assume that component A is comprised of components A and D, and component B is component B plus component C. The vA 351 system is now  $\mathcal{M}_{AD} = 1.14M_{\odot}$  and  $\mathcal{M}_{BC} = 0.91M_{\odot}$ .
5. We have achieved our second goal, that of establishing component masses. Combining  $V$  and  $K$  photometry with a parallax derived from our astrometry,  $\mathcal{M}_{AD}$ ,  $\mathcal{M}_{BC}$ , the AD - BC magnitude difference,  $\mathcal{M}_C/\mathcal{M}_B$  mass ratio from absorption

line RVs, an estimate for interstellar absorption, M dwarf Luminosity-Mass relations, and a WD Luminosity-Mass relation for an assumed Hyades age of 670 My we solve for individual component masses that would best satisfy all the priors. We find  $\mathcal{M}_A = 0.53 \pm 0.10M_{\odot}$ ,  $\mathcal{M}_B = 0.43 \pm 0.04M_{\odot}$ ,  $\mathcal{M}_C = 0.41 \pm 0.04M_{\odot}$ , and  $\mathcal{M}_D = 0.54 \pm 0.04M_{\odot}$ . The WD mass,  $\mathcal{M}_D$ , comes only from the  $K$ -band photometry. Including an extinction,  $A_V = 0.6$ , lowers the Table 11 fit residuals, improving the consistency between the  $V$  and  $K$  solutions, yielding  $\mathcal{M}_A = 0.56 \pm 0.07M_{\odot}$ ,  $\mathcal{M}_B = 0.46 \pm 0.01M_{\odot}$ ,  $\mathcal{M}_C = 0.44 \pm 0.01M_{\odot}$ , and  $\mathcal{M}_D = 0.53 \pm 0.04M_{\odot}$ .

6. The  $\mathcal{M}_C$  and  $\mathcal{M}_B$ , the parallax, and the absorption line RV amplitudes,  $K_B$  and  $K_C$ , yield an inclination,  $i_{BC} \simeq 23^\circ$  and separation,  $a_{BC} \simeq 0.016$  AU, consistent with an observed  $v \sin i = 11 \pm 2$  km  $s^{-1}$ , and plausible B and C radii.
7. Periodograms of the TRANS mode astrometric residuals provide extremely weak evidence for a  $P_{AD} \sim 25^{\text{d}}$ . The component A RV AD-BC orbit residuals exhibit a strong peak in the periodogram at  $P_{AD} \sim 21^{\text{d}}$ .
8. The spectra show H $\alpha$  in emission with from two to four components. The centrally located (in RV) components 2 and 3 are associated with the AD components, and may be caused by self absorption in a circumbinary hydrogen cloud. The amplitudes of the B and C RVs place emission further from the BC system barycenter.
9. We see HeI ( $\lambda$  5876.6Å) in emission with from one to three components. We identify component B and C emission from RV behavior, which in this case more closely tracks the absorption line RVs. Hence, we surmise a location for two of the HeI components closer to the surfaces of B and C than the H $\alpha$  emission. The RV behavior of the central HeI component supports association with the AD components of the system.
10. Only partially achieving our third goal, a qualitative model explaining all observed phenomena, we propose hypotheses that will require future observations and theoretical interpretation for completion.

Some future *Gaia* catalog could contain AD-BC orbital parameters and confirm the total system mass. However, the very small magnitude difference between the AD and BC pairs could make that determination problematical. Additional low-cadence monitoring of the system with speckle techniques could further improve the AD-BC orbit. vA 351 remains a phenomena-rich laboratory for future magnetohydrodynamic model testing.

Support for GFB, OGF, and BEM for this work was provided by NASA through grants GTO-4892, 5657; and GO-6479, 6881 from the Space Telescope Science Institute, which is operated by the Association of Universities for Research in Astronomy, Inc., under NASA contract NAS5-26555. GT acknowledges partial support from the

NSF through grant AST-1509375. Similarly, EPH acknowledges support from the NSF through grants AST-1517824 and AST-1909560 for the analysis of the speckle data.

This publication makes use of data products from the Two Micron All Sky Survey, which is a joint project of the University of Massachusetts and the Infrared Processing and Analysis Center/California Institute of Technology, funded by NASA and the NSF. This research has made use of the SIMBAD and VizieR databases and Aladin, operated at CDS, Strasbourg, France, the NASA/IPAC Extragalactic Database (NED) which is operated by JPL, California Institute of Technology, under contract with the NASA, and NASA's Astrophysics Data System Abstract Service. We acknowledge the essential contribution of the WD cooling models Web site (<http://www.astro.umontreal.ca/~bergeron/CoolingModels>).

This work has made use of data from the European Space Agency (ESA) mission *Gaia* (<https://www.cosmos.esa.int/gaia>), processed by the *Gaia* Data Processing and Analysis Consortium (DPAC, <https://www.cosmos.esa.int/web/gaia/dpac/consortium>). Funding for the DPAC has been provided by national institutions, in particular the institutions participating in the *Gaia* Multilateral Agreement.

We thank Art Bradley and Linda Abramowicz-Reed for their unflagging and expert *FGS* instrumental support over the last 25 years. Cassegrain Echelle (CE) Spectrograph observing and data reduction assistants included J. Crawford, Aubra Anthony, Iskra Strateva, Tim Talley, Amber Armstrong, Robert Hollingsworth, Casey Kyte, and Jacob Bean. We thank Dave Doss, John Booth, and many other support personnel at McDonald Observatory for their cheerful assistance over many years. Thank you Ray Lucas for morale-building violin playing during a particularly productive observing run! GFB thanks Chick Woodward and Nancy Morrison for the suggestion of self-absorption to explain the central H $\alpha$  peaks. We thank Team IGRINS, especially Greg Mace and Heeyoung Oh for getting an April 2019 DCT observation. We thank Gerard van Belle, Catherine Clark, and Zachary Hartman at Lowell who battled difficult weather conditions to secure the February 2020 speckle observation.

The American Astronomical Society supported the preparation of this paper as GFB carried out his duties as Society Secretary. For this he is sincerely grateful. GFB fondly remembers Debbie Winegarten (R.I.P.), whose able assistance with Secretarial matters freed me to devote time to this analysis.

We thank an anonymous referee for a careful and useful assessment, improving the final paper.

## APPENDIX

### A Cautionary Tale

There exist many pitfalls between data and definitive orbit determination, some rather entertainingly recounted in van den Bos (1962). We managed to find a few more in producing our vA 351 result. In a few years *Gaia* will flood us with perturbations crying out for orbit determination. Our experience may prove instructive.

For an embarrassingly long period of time, we worked with an AD-BC astrometric orbit solution (Figure 26) that produced severe cognitive dissonance, to the point that two of us (LP, OGF) strongly, and correctly objected to paper submission. The astrometry and the RVs were inconsistent with each other. As seen in Figure 3, the RVs were basically flat line except for a very few epochs. In retrospect this is easily explained by the highly eccentric AD-BC orbit. Even though one of us (GFB) checked and rechecked the RVs, they refused to make sense, given our acceptance of the Figure 26 orbit. However, one of us (EH) explored the consequences of component misidentification (for many epochs swapping AD for BC, essentially changing the measured position angle by 180°) and proposed the Figure 1 orbit, having an orbital period half that previously determined, which the RVs (Figure 3) immediately confirmed (GT).

Take care with component identification, particularly for near equal brightness systems with component brightness variability. Always explore alternate possibilities. Believe rechecked RVs. If possible, always appeal to more than one observational technique. RVs and astrometry together made the proper orbit identification possible. Intriguingly, the final component masses obtained from analyses based on either orbit agree within their respective errors. But, Figure 1 and Table 11 describe the real vA 351 system.

## REFERENCES

- Alonso-Floriano F.J., Morales J.C., Caballero J.A., et al., 2015. *A&A*, 577, A128
- An D., Terndrup D.M., & Pinsonneault M.H., 2007. *ApJ*, 671, 1640
- Belokurov V., Penoyre Z., Oh S., et al., 2020. *MNRAS*, 496, 1922
- Benedict G.F., Henry T.J., Franz O.G., et al., 2016. *AJ*, 152, 141
- Benedict G.F., McArthur B., Chappell D.W., et al., 1999. *AJ*, 118, 1086
- Benedict G.F., McArthur B., Nelan E., et al., 1998. *AJ*, 116, 429
- Benedict G.F., McArthur B.E., Feast M.W., et al., 2007. *AJ*, 133, 1810
- Benedict G.F., McArthur B.E., Feast M.W., et al., 2011. *AJ*, 142, 187
- Benedict G.F., McArthur B.E., Franz O.G., et al., 2001. *AJ*, 121, 1607
- Benedict G.F., McArthur B.E., Nelan E.P., et al., 2017. *PASP*, 129, 012001
- Bergeron P., Wesemael F., Dufour P., et al., 2011. *ApJ*, 737, 28
- Boyajian T.S., von Braun K., van Belle G., et al., 2012. *ApJ*, 757, 112
- Brown T.M., Latham D.W., Everett M.E., et al., 2011. *AJ*, 142, 112
- Cox A.N., 2000. *Allen's Astrophysical Quantities*. AIP Press
- de Bruijne J.H.J., Hoogerwerf R., & de Zeeuw P.T., 2001. *A&A*, 367, 111
- D'Elia V., Perri M., Puccetti S., et al., 2013. *A&A*, 551, A142
- Donati J.F., Morin J., Petit P., et al., 2008. *MNRAS*, 390, 545
- Franz O.G., Henry T.J., Wasserman L.H., et al., 1998a. *AJ*, 116, 1432

- Franz O.G., Wasserman L.H., Benedict G.F., et al., 1998b. In *American Astronomical Society Meeting Abstracts*, vol. 30 of *Bulletin of the American Astronomical Society*, 1402
- Franz O.G., Wasserman L.H., Bradley A.J., et al., 1994. In *American Astronomical Society Meeting Abstracts #184*, vol. 184, 43.01
- Gaia Collaboration, Brown, A. G. A., Vallenari, A., et al., 2018. *A&A*  
URL <https://doi.org/10.1051/0004-6361/201833051>
- Gaia Collaboration, van Leeuwen F., Vallenari A., et al., 2017. *A&A*, 601, A19
- Gehrels N., Chincarini G., Giommi P., et al., 2004. *ApJ*, 611, 1005
- Gómez Maqueo Chew Y., Stassun K.G., Prša A., et al., 2012. *ApJ*, 745, 58
- Gossage S., Conroy C., Dotter A., et al., 2018. *ApJ*, 863, 67
- Hanson R.B., 1975. *AJ*, 80, 379
- Harrison T.E., McNamara B.J., Szkody P., et al., 1999. *ApJ*, 515, L93
- Hartmann L.W., Soderblom D.R., & Stauffer J.R., 1987. *AJ*, 93, 907
- Henry T.J., Franz O.G., Wasserman L.H., et al., 1999. *ApJ*, 512, 864
- Holberg J.B. & Bergeron P., 2006. *AJ*, 132, 1221
- Horch E.P., Bahi L.A.P., Gaulin J.R., et al., 2012. *AJ*, 143, 10
- Horch E.P., Casetti-Dinescu D.I., Camarata M.A., et al., 2017. *AJ*, 153, 212
- Horch E.P., van Belle G.T., Davidson Jr. J.W., et al., 2015. *AJ*, 150, 151
- Kowalski A.F. & Allred J.C., 2018. *ApJ*, 852, 61
- Kowalski P.M. & Saumon D., 2006. *ApJ*, 651, L137
- Lee J.J., Gullikson K., & Kaplan K., 2017. *Igrins/Plp 2.2.0*
- Lindgren L., Klioner S.A., Hernández J., et al., 2020. *arXiv e-prints*, arXiv:2012.03380
- Mace G., Jaffe D., Park C., et al., 2016. In *19th Cambridge Workshop on Cool Stars, Stellar Systems, and the Sun (CS19)*, 55
- Mann A.W., Feiden G.A., Gaidos E., et al., 2015. *ArXiv e-prints*
- McArthur B.E., Benedict G.F., Harrison T.E., et al., 2011. *AJ*, 141, 172
- McCarthy J.K., Sandiford B.A., Boyd D., et al., 1993. *PASP*, 105, 881
- Morin J., Donati J.F., Petit P., et al., 2008. *MNRAS*, 390, 567
- Morin J., Donati J.F., Petit P., et al., 2010. *MNRAS*, 407, 2269
- Morin J., Donati J.F., Petit P., et al., 2011. In D. Prasad Choudhary & K.G. Strassmeier, eds., *Physics of Sun and Star Spots*, vol. 273, 181–187
- Naos S., 2016. *Annual Review of Astronomy and Astrophysics*, 54, 441
- Naos S. & Fabrycky D.C., 2014. *ApJ*, 793, 137
- Newton E.R., Irwin J., Charbonneau D., et al., 2017. *ApJ*, 834, 85
- Pavlenko Y.V., Suarez Mascareno A., Zapatero Osorio M.R., et al., 2019. *arXiv e-prints*, arXiv:1905.07347
- Perryman M.A.C., Brown A.G.A., Lebreton Y., et al., 1998. *A&A*, 331, 81
- Pourbaix D. & Jorissen A., 2000. *A&AS*, 145, 161
- Prato L., 2007. *ApJ*, 657, 338
- Roeser S., Demleitner M., & Schilbach E., 2010. *AJ*, 139, 2440
- Salaris M. & Bedin L.R., 2018. *Monthly Notices of the Royal Astronomical Society*, 480, 3170
- Schlafly E.F. & Finkbeiner D.P., 2011. *ApJ*, 737, 103
- Semaan T., Hubert A.M., Zorec J., et al., 2013. *A&A*, 551, A130
- Skrutskie M.F., Cutri R.M., Stiening R., et al., 2006. *AJ*, 131, 1163
- Standish Jr. E.M., 1990. *A&A*, 233, 252
- Stassun K.G. & Torres G., 2021. *arXiv e-prints*, arXiv:2101.03425
- Stauffer J.R., Balachandran S.C., Krishnamurthi A., et al., 1997. *ApJ*, 475, 604
- Taylor B.J., 2006. *AJ*, 132, 2453
- Tody D., 1993. In R.J. Hanisch, R.J.V. Brissenden, & J. Barnes, eds., *Astronomical Data Analysis Software and Systems II*, vol. 52 of *Astronomical Society of the Pacific Conference Series*, 173
- Tremblay P.E., Bergeron P., & Gianninas A., 2011. *ApJ*, 730, 128
- van Bueren H.G., 1952. *Bulletin of the Astronomical Institutes of the Netherlands*, 11, 385
- van den Bos W.H., 1962. *PASP*, 74, 297
- Wright E.L., Eisenhardt P.R.M., Mainzer A.K., et al., 2010. *AJ*, 140, 1868
- Zucker S., Torres G., & Mazeh T., 1995. *ApJ*, 452, 863

TABLE 1  
VA 351 COMPONENT B RELATIVE TO COMPONENT A SEPARATIONS, POSITION ANGLES,  
RESIDUALS,  $\Delta m$ , AND SOURCES

	mJD	$\rho$ (mas)	$\delta\rho^a$ (mas)	$\theta$ (deg)	$\delta\theta$ (deg)	$\rho\delta\theta$ (mas)	$\Delta m^b$ (mag)	Sources
1	49396.6222	51.2	0.0	291.50	0.41	0.37	-0.04	<i>FGS3</i>
2 <sup>c</sup>	49396.6222	38.9	10.0	184.61	-24.86	-18.02	-0.04	<i>FGS3</i>
3	50082.4521	79.6	-0.2	257.89	-4.51	-6.27	0.06	<i>FGS3</i>
4	50128.8754	81.9	2.9	264.88	-0.67	-0.96	0.08	<i>FGS3</i>
5	50160.0312	78.8	1.2	267.69	-0.17	-0.24	-0.04	<i>FGS3</i>
6	50375.0539	52.7	-0.3	289.28	-0.26	-0.24	0.01	<i>FGS3</i>
7	50437.9500	38.8	-0.1	302.69	-0.22	-0.15	0.00	<i>FGS3</i>
8	50457.8196	33.1	-0.3	308.82	-0.91	-0.53	-0.08	<i>FGS3</i>
9	50481.6339	25.8	0.0	320.95	-1.02	-0.46	-0.54	<i>FGS3</i>
10	50650.4159	43.8	1.2	218.85	-0.96	-0.74	0.13	<i>FGS3</i>
11	50751.4075	62.0	0.6	236.22	-0.38	-0.41	0.00	<i>FGS3</i>
12	51033.4170	82.3	2.1	263.99	3.99	5.75	0.02	<i>FGS3</i>
13	51111.4344	80.2	1.6	270.35	4.96	6.96		<i>FGS3</i>
14	56933.5560	80.0	-0.4	257.52	-0.41	-0.58	-0.25	speckle
15	56936.5145	79.0	-1.4	258.12	-0.01	-0.02	0.00	speckle
16	56969.4600	78.0	-2.5	259.72	-0.72	-0.99	-0.01	speckle
17	56970.4462	80.0	-0.6	260.92	0.46	0.64	-0.03	speckle
18 <sup>c</sup>	58888.1125	73.0	-5.6	263.70	8.61	11.06	-0.04	speckle
						0.06		CfA spectra

<sup>a</sup> All  $\delta$  values are observed minus calculated (O-C) from the Table 2 orbit.

<sup>b</sup> Magnitude difference between components AD and BC. For *FGS3*  $\Delta F583W \simeq \Delta V$  (Henry et al. 1999). For speckle,  $\Delta\lambda 692\text{nm}$  (Horch et al. 2012). For CfA spectra see Section 3.4. Observations #9 and #14 detect flaring activity from one of the M dwarf components.

<sup>c</sup> Observations omitted from final Table 2 orbit.

TABLE 2  
PARAMETERS FOR VA 351 AD-BC RELATIVE ORBIT

Parameter	Units	Value	err
P	days	987.9	1.4
P	years	2.705	0.004
$T_0$	mJD	51522.4	2.5
ecc		0.790	0.006
$\omega_{AD}$	°	149	13
$a$	mas	45.4	0.6
inc	°	14	8
$\Omega$	°	289.5	0.9

TABLE 3  
CE ABSORPTION LINE RADIAL VELOCITIES<sup>a</sup>

mJD <sup>b</sup>	VA	VAerr	VB	VBerr	VC	VCerr	$\Phi(\text{BC})^c$	$\Phi(\text{AD-BC})^d$
49962.4226	41.16	0.17	75.33	0.44	4.51	0.44	0.6424	0.7536
50090.1532	40.92	0.14	10.18	0.32	71.84	0.4	0.1227	0.8175
50090.2080	40.67	0.17	-1.6	0.39	83.71	0.54	0.1958	0.8175
50090.2517	41.02	0.26	-3.73	0.45	86.77	0.68	0.2541	0.8176

<sup>a</sup> Full table available electronically. All velocity units in  $\text{km s}^{-1}$ .

<sup>b</sup> mJD=JD-2400000.5

<sup>c</sup> BC orbit phase

<sup>d</sup> AD-BC orbit phase

TABLE 4  
CFA ABSORPTION LINE RADIAL VELOCITIES<sup>a</sup>

mJD <sup>b</sup>	VA	VAerr	VB	VBerr	VC	VCerr	$\Phi(\text{BC})^c$	$\Phi(\text{AD-BC})^d$
46428.1524	41.63	1.72	50.69	3.2	30.28	3.72	0.5008	0.9848
46449.2532	40.4	1.68	81.07	3.12	-7.05	3.63	0.6638	0.9953
47436.3954	40.47	2.11	-5.45	3.92	82.31	4.56	0.1888	0.4894
47436.4072	41.43	2.03	-6.53	3.77	88.74	4.38	0.2046	0.4894
48281.1881	42.37	1.95	86.51	3.63	-8.87	4.22	0.7219	0.9122

<sup>a</sup> Full table available electronically. All velocity units in  $\text{km s}^{-1}$ .

<sup>b</sup> mJD=JD-2400000.5

<sup>c</sup> BC orbit phase

<sup>d</sup> AD-BC orbit phase

TABLE 5  
OTHER ABSORPTION LINE RADIAL VELOCITIES

mJD <sup>a</sup>	VA	VAerr	VB	VBerr	VC	VCerr	$\Phi(\text{BC})^b$	$\Phi(\text{AD-BC})^c$
57441.1134 <sup>d</sup>	33	1.5	2.4	1.5	88.4	1.5	0.3476	0.4965
57443.0777 <sup>d</sup>	29.2	1.5	61.6	1.5	29.2	1.5	0.9694	0.4975
58584.1012 <sup>d</sup>	37.65	1.39	75.54	0.53	0.51	0.9	0.8777	0.0924
49672.3000 <sup>e</sup>	37	1	22	1	59	1	0.4198	0.6084
49732.0700 <sup>e</sup>	38	1	-1	1	82	1	0.1940	0.6383
46388.5 <sup>f</sup>	41.4	1.5					0.5759	0.9649

<sup>a</sup> mJD=JD-2400000.5

<sup>b</sup> BC orbit phase

<sup>c</sup> AD-BC orbit phase

<sup>d</sup> from IGRINS

<sup>e</sup> from Stauffer et al. (1997), errors assumed

<sup>f</sup> from Hartmann et al. (1987)

TABLE 6  
RV BC ORBIT

Parameter	B	err	C	err
<u>Absorption Lines<sup>a</sup></u>				
P [days]	0.7492425	0.0000003		
T <sub>0</sub> [mJD]	50367.09409	0.0005		
K [km s <sup>-1</sup> ]	43.76	0.15	46.29	0.17
ecc	0	0.002		
$\gamma$ [km s <sup>-1</sup> ]	40.2	0.2		
$\omega$ <sup>[b]</sup>	-	-		
Derived				
$K_B/K_C = \mathcal{M}_C/\mathcal{M}_B$	0.945	0.005		
<u>H<math>\alpha</math> Emission Lines<sup>b</sup></u>				
K [km s <sup>-1</sup> ]	62.93	0.64	64.05	0.69
ecc	0	0.002		
$\omega$ <sup>[c]</sup>	-	-	-	-
$\gamma$ [km s <sup>-1</sup> ]	40.45	0.40		
Derived				
$K_B/K_C = \mathcal{M}_C/\mathcal{M}_B$	0.982	0.015		
<u>He I Emission Lines<sup>c</sup></u>				
K [km s <sup>-1</sup> ]	44.41	0.38	45.15	0.37
$\gamma$ [km s <sup>-1</sup> ]	41.1	0.5		
Derived				
$K_B/K_C = \mathcal{M}_C/\mathcal{M}_B$	0.984	0.011		

<sup>a</sup> Section 3

<sup>b</sup> Section 7.1

<sup>c</sup> Section 7.2

TABLE 7  
RV ORBITAL ELEMENTS FOR VA 351 AD-BC

Parameter	Units	Value	err
$P$	days	987.3	1.8
$P$	years	2.703	0.005
$T_0$	JD-2400000	51518	8
$e$	-	0.81	0.01
$\omega_{AD}$	°	149.2	2.8
$K_A$	km s <sup>-1</sup>	3.98	0.11
$\gamma_{AD-BC}$	km s <sup>-1</sup>	40.64	0.05

TABLE 8  
VA 351 REFERENCE STAR *Gaia* INPUT AND FINAL PARALLAXES<sup>a</sup>

Ref Star #	$V$	$B - V$	DR2 Source	$G$	$\varpi$	err	Final $\varpi$	err
2	11.79	0.73	3313958012105540000	11.79	4.74	0.06	4.73	0.03
3	13.88	0.98	3313956534636790000	13.84	2.17	0.04	2.17	0.02
4	11.84	1.64	3313957423693360000	11.56	0.23	0.07	0.23	0.04
5	14.37	1.24	3313958252623700000	14.31	0.23	0.04	0.22	0.02

<sup>a</sup> Parallax and errors in mas.

TABLE 9  
REFERENCE FRAME STATISTICS, VA 351 PARALLAX, AND  
PROPER MOTION

Parameter	Value
TRANS+speckle time span	26.99 y
number of observation sets	18
POS mode time span	1.8 y
number of observation sets	7
POS reference star $\langle V \rangle$	13.31
POS reference star $\langle (B - V) \rangle$	1.14
<i>HST</i> Absolute $\varpi$	$18.37 \pm 0.65$ mas
Relative $\mu_\alpha$	$108.7 \pm 0.9$ mas yr <sup>-1</sup>
Relative $\mu_\delta$	$-21.9 \pm 1.3$ mas yr <sup>-1</sup>
$\vec{\mu} = 110.9$ mas yr <sup>-1</sup>	
P.A. = 101°4	
<i>Gaia</i> DR2 Absolute $\varpi$	$20.10 \pm 0.15$ mas
Absolute $\mu_\alpha$	$114.77 \pm 0.31$ mas yr <sup>-1</sup>
Absolute $\mu_\delta$	$-25.28 \pm 0.20$ mas yr <sup>-1</sup>
$\vec{\mu} = 117.52$ mas yr <sup>-1</sup>	
P.A. = 102°4	
<i>Gaia</i> EDR3 Absolute $\varpi$	$19.31 \pm 0.19$ mas
Absolute $\mu_\alpha$	$107.26 \pm 0.21$ mas yr <sup>-1</sup>
Absolute $\mu_\delta$	$-27.19 \pm 0.20$ mas yr <sup>-1</sup>
$\vec{\mu} = 110.65$ mas yr <sup>-1</sup>	
P.A. = 104°2	



TABLE 10  
ORBITAL ELEMENTS FOR VA 351 AD-BC

Parameter	Units	Value	err
$P$	days	988.0	1.5
$P$	years	2.705	0.004
$T_0$	JD-2400000	51522	3
$e$	-	0.790	0.007
$\omega$	$^\circ$	149	12
$i$	$^\circ$	14	8
$\Omega^a$	$^\circ$	289.5	1.0
$\alpha_A$	mas	20.1	0.9
$a$	mas	45.4	0.6
Derived Parameters			
$\mathcal{M}_{tot}$	$\mathcal{M}_\odot$	2.06	0.24
$f^b$	-	0.443	0.022
$\alpha_A$	AU	1.09	0.07
$a$	AU	2.47	0.09
$\mathcal{M}_{AD}$	$\mathcal{M}_\odot$	1.14	0.14
$\mathcal{M}_{BC}$	$\mathcal{M}_\odot$	0.91	0.11

<sup>a</sup> Equinox 2000.0

<sup>b</sup> Mass fraction from Equation 9.

TABLE 11  
DISSECTING VA 351

line #					
		<b>Input Data from Photometry</b>			
1	total apparent magnitude	$V$	$K$	$V - K$	
2	total intensity	$13.27 \pm 0.03$	$8.268 \pm 0.029$	$5.00 \pm 0.04$	
3	AD - BC $\Delta$ mag	$0.0492 \pm 0.0012$	$4.929 \pm 0.017$		
4	estimated absorption, $A_{V,K}^a$	$0 \pm 0.1$	$0 \pm 0.03$		
		<b>Input Data from RVs</b>			
5	$\mathcal{M}_C/\mathcal{M}_B^b$	$0.945 \pm 0.005$			
		<b>Input Data from Astrometry</b>			
6	$\mathcal{M}_B + \mathcal{M}_C$	$0.91 \pm 0.11 \mathcal{M}_\odot$			
7	$(\mathcal{M}_A + \mathcal{M}_D)/(\mathcal{M}_B + \mathcal{M}_C)$	$1.26 \pm 0.22$			
8	$\mathcal{M}_A + \mathcal{M}_D$	$1.14 \pm 0.14 \mathcal{M}_\odot$			
9	$\varpi_{\text{abs}}$	$18.4 \pm 0.7$ mas			
10	$\mathcal{M}_{\text{tot}}$	$2.06 \pm 0.24 \mathcal{M}_\odot$			
		<b>Parameters<sup>c</sup></b>			
		$V$	$K$		
11	Component Intensities				
	A	0.02300	2.45858		
12	B	0.01363	1.30917		
13	C	0.01107	1.15657		
14	D	0.00164	0.00519		
		System Parallax			
15	$\varpi_{\text{abs}}$	18.15 mas	18.34 mas		
		System Absorption			
16	$A_{V,K}$	0.04 mag	0.00 mag		
		<b>Final Values and Residuals<sup>d</sup></b>			
		$V$	res	$K$	res
17	total intensity	0.0493	0.00001	4.929	+0.00004
18	AD - BC $\Delta$ mag	0.0	-0.002	0.00	0.001
19	$\mathcal{M}_C/\mathcal{M}_B$	0.945	0.000	0.9454	0.000
20	$\mathcal{M}_B + \mathcal{M}_C$	$0.78 \mathcal{M}_\odot$	-0.13	$0.90 \mathcal{M}_\odot$	-0.014
21	$(\mathcal{M}_A + \mathcal{M}_D)/(\mathcal{M}_B + \mathcal{M}_C)$	1.28	0.02	1.27	0.02
22	$\mathcal{M}_A + \mathcal{M}_D$	$1.00 \mathcal{M}_\odot$	-0.15	$1.14 \mathcal{M}_\odot$	-0.002
23	$\varpi_{\text{abs}}$	18.15	0.2	18.34	0.04
24	$\mathcal{M}_{\text{tot}}$	$1.78 \mathcal{M}_\odot$	-0.28	$2.04 \mathcal{M}_\odot$	-0.01
25	$\sum(\text{resid}^2)$		4.227		0.029
		<b>Final Magnitudes</b>			
		component	$V$	$K$	
26	A		14.09	9.02	
27	B		14.66	9.71	
28	C		14.89	9.84	
29	D		16.96	15.71	
30	Total		13.26	8.27	
		<b>Final Absolute Magnitudes<sup>e</sup></b>			
		component	$M_V$	$M_K$	$V - K$
31	A		10.35	5.34	5.01
32	B		10.92	6.02	4.89
33	C		11.14	6.16	4.98
34	D		13.21	12.03	+1.18
35	Total		9.52	4.58	4.94
		<b>Final Masses<sup>d</sup></b>			
		component	$V$ -band fit	$K$ -band fit	av
36	$\mathcal{M}_A$		$0.46 \mathcal{M}_\odot$	$0.60 \mathcal{M}_\odot$	$0.53 \pm 0.10 \mathcal{M}_\odot$
37	$\mathcal{M}_B$		$0.40 \mathcal{M}_\odot$	$0.46 \mathcal{M}_\odot$	$0.43 \pm 0.04 \mathcal{M}_\odot$
38	$\mathcal{M}_C$		$0.38 \mathcal{M}_\odot$	$0.44 \mathcal{M}_\odot$	$0.41 \pm 0.04 \mathcal{M}_\odot$
39	$\mathcal{M}_D$		-	$0.53 \mathcal{M}_\odot$	$0.54 \pm 0.04 \mathcal{M}_\odot$
40	$\mathcal{M}_{\text{tot}}$		$1.78 \mathcal{M}_\odot$	$2.04 \mathcal{M}_\odot$	$1.91 \pm 0.13 \mathcal{M}_\odot$

<sup>a</sup> Our initial estimate is near .<sup>b</sup> From absorption line RVs, Table 6.<sup>c</sup> Final values varied to minimize **line 17-24** residuals.<sup>d</sup> After least squares "fit".<sup>e</sup> Absorption-corrected.

TABLE 12  
RESTRICTED EXPRESSIONS FOR MASS AS A FUNCTION OF  
ABSOLUTE MAGNITUDE

Param	$M_V^a$	$M_K^a$	WD $M_K^b$
C0	1.4594±0.0004	2.47±0.25	0.197±0.016
C1	-0.09693 0.00058	-0.4768 0.0781	0.198 0.075
C2	-	0.0237 0.0059	0.562 0.096
C3	-	-	-0.206 0.033
X <sub>0</sub>	-	-	11.35

<sup>a</sup> Parameters in the Equation 10 polynomial.

<sup>b</sup> Parameters in the Equation 11 polynomial.

TABLE 13  
H $\alpha$  EQUIVALENT WIDTHS<sup>a</sup>

mJD <sup>b</sup>	$\Phi_{BC}$	$\Phi_{AD-BC}$	EWtot	err	EW1	err	EW2	err	EW3	err	EW4	err
49962.4226	0.8930	0.42452	-6.65	0.20	-0.92	0.05	-2.21	0.16	-2.71	0.05	-0.80	0.09
50090.1532	0.3726	0.55390	-5.80	0.20	-0.96	0.06	-2.29	0.13	-2.03	0.09	-0.52	0.10
50090.208	0.4458	0.55395	-5.92	0.15	-0.98	0.05	-2.01	0.14	-2.16	0.04	-0.76	0.04
50090.2517	0.5041	0.55400	-6.43	0.13	-1.11	0.05	-2.22	0.11	-2.25	0.04	-0.86	0.04
50091.112	0.6523	0.55487	-6.36	0.14	-0.79	0.06	-2.62	0.06	-2.33	0.07	-0.62	0.09
50091.1417	0.6920	0.55490	-7.16	0.13	-1.22	0.07	-2.48	0.06	-2.47	0.07	-0.98	0.06
50091.1662	0.7247	0.55492	-6.18	0.10			-3.10	0.07	-3.09	0.07		

<sup>a</sup> Full table available electronically. Equivalent widths in  $\text{\AA}$

<sup>b</sup> mJD=JD-2400000.5

TABLE 14  
COMPONENT B,C RADIAL VELOCITIES FROM H $\alpha$ <sup>a</sup>

mJD	$\Phi_{BC}$	$\Phi_{AD-BC}$	B	err	C	err
49962.4226	0.8930	0.42452	101.48	3.58	-14.21	1.83
50090.1532	0.3726	0.55390	-10.09	1.70	90.97	5.46
50090.2080	0.4458	0.55395	-12.31	3.02	100.07	1.31
50090.2517	0.5041	0.55400	-15.35	2.32	103.08	1.15
50091.1120	0.6523	0.55487	-7.75	1.25	84.05	2.18
50091.1417	0.6920	0.55490	-53.97	1.07	61.73	1.57
50364.4174	0.4279	0.83169	-11.90	2.99	100.78	1.75
50366.3739	0.0392	0.83367	105.98	0.80	-15.77	2.25

<sup>a</sup> Full table available electronically. All velocity units in  $\text{km s}^{-1}$ .

TABLE 15  
COMPONENT V2, V3 RADIAL VELOCITIES FROM H $\alpha$ <sup>a</sup>

mJD	$\Phi_{BC}$	$\Phi_{AD-BC}$	V2	err	V3	err
49962.4226	0.8930	0.42452	20.25	0.82	57.08	0.84
50090.1532	0.3726	0.55390	22.13	0.91	55.5	1.05
50090.2080	0.4458	0.55395	22.36	0.64	59.62	0.51
50090.2517	0.5041	0.55400	21.79	0.68	60.24	0.63
50091.1120	0.6523	0.55487	25.25	0.62	56.16	0.97
50091.1662	0.7247	0.55492	24.49	0.38	56.19	0.39
50364.4174	0.4279	0.83169	22	0.95	59.51	0.8
50365.3997	0.7390	0.83269	24.26	0.34	55.43	0.38

<sup>a</sup> Full table available electronically. All velocity units in  $\text{km s}^{-1}$ .

TABLE 16  
HE I EQUIVALENT WIDTHS<sup>a</sup>

mJD <sup>b</sup>	$\Phi_{BC}$	$\Phi_{AD-BC}$	EW <sub>tot</sub>	err	EW <sub>B</sub>	err	EW <sub>2</sub>	err	EW <sub>C</sub>	err
49962.4226	0.8930	0.42452	-1.02	0.11	-0.29	0.06	-0.39	0.06	-0.34	0.06
50090.1532	0.3726	0.55390	-1.28	0.05	-0.61	0.03	-0.27	0.03	-0.12	0.03
50090.2080	0.4458	0.55395	-1.31	0.11	-0.34	0.07	-0.65	0.06	-0.24	0.05
50090.2517	0.5041	0.55400	-1.43	0.07	-0.20	0.04	-0.92	0.04	-0.31	0.04
50091.1120	0.6523	0.55487	-1.39	0.09	-0.23	0.06	-0.76	0.04	-0.40	0.05
50091.1662	0.7247	0.55492	-0.97	0.07			-0.97	0.07		
50404.2830	0.6358	0.87207	-2.19	0.15	-0.61	0.09	-0.69	0.09	-0.88	0.08
50404.3080	0.6692	0.87210	-0.96	0.07			-0.96	0.07		
50404.3360	0.7065	0.87213	-1.99	0.17	-0.65	0.10	-0.85	0.10	-0.49	0.10

<sup>a</sup> Full table available electronically. Equivalent widths in  $\text{\AA}$

<sup>b</sup> mJD=JD-2400000.0

TABLE 17  
HE I EMISSION LINE RVs <sup>a</sup>

mJD <sup>b</sup>	$\Phi_{BC}$	$\Phi_{AD-BC}$	VB	err	V <sub>cen</sub>	err	VC	err
49962.4226	0.8930	0.42452	-1.6	4.5	45.4	3.5	95.0	3.6
50090.1532	0.3726	0.55390	72.5	2.0	39.6	1.0	2.4	2.0
50090.2080	0.4458	0.55395	86.8	4.8	37.1	0.9	-2.3	1.6
50090.2517	0.5041	0.55400	83.2	2.8	42.8	0.6	-1.5	1.7
50091.1120	0.6523	0.55487	77.0	1.9	44.5	1.1	3.5	1.2
50091.1662	0.7247	0.55492			44.4	1.2		
50404.2830	0.6358	0.87207	65.2	3.3	25.0	2.7	-34.2	1.4
50404.3080	0.6692	0.87210			36.2	1.3		
50404.3360	0.7065	0.87213	54.8	1.0	39.4	0.8	20.1	1.2

<sup>a</sup> Full table available electronically. All velocity units in  $\text{km s}^{-1}$ .

TABLE 18  
 SWIFT-XRT DETECTIONS OF VA 351

mJD	$\Phi_{BC}$	$\Phi_{AD-BC}$	X-ray Flux <sup>a</sup>	S/N
53832.8833	0.790	0.9884	1.78E-12	6.1
54162.0951	0.183	0.3218	1.80E-12	11
54437.1163	0.248	0.6004	1.27E-12	8.8

<sup>a</sup> 0.3-10 keV flux in units  $\text{mW m}^{-2}$

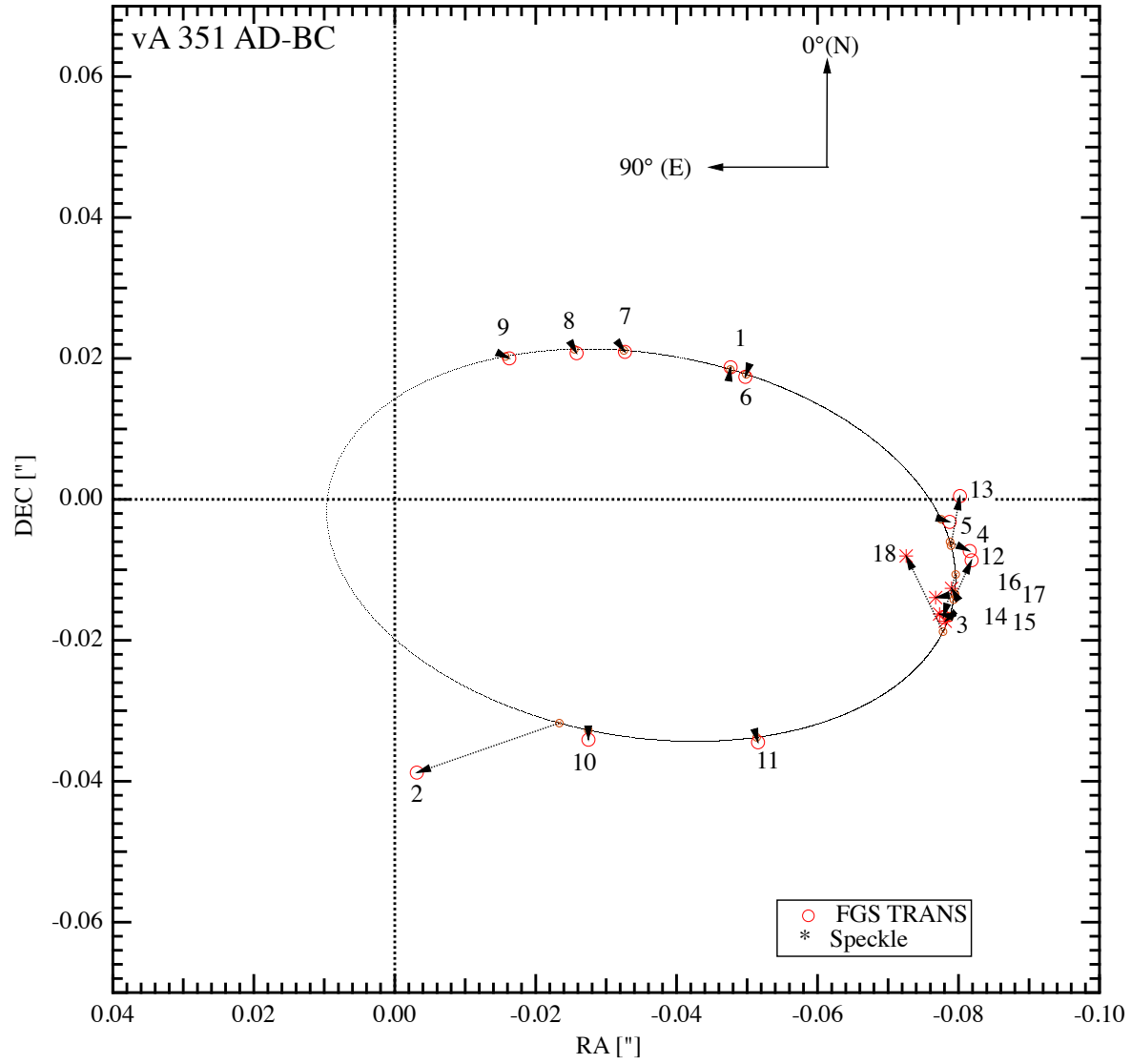


FIG. 1.— A relative orbit AD-BC for vA 351 derived from FGS TRANS and ground-based speckle observations. We plot observation numbers from Table 1. We omitted observations 2 and 18 for the final solution.

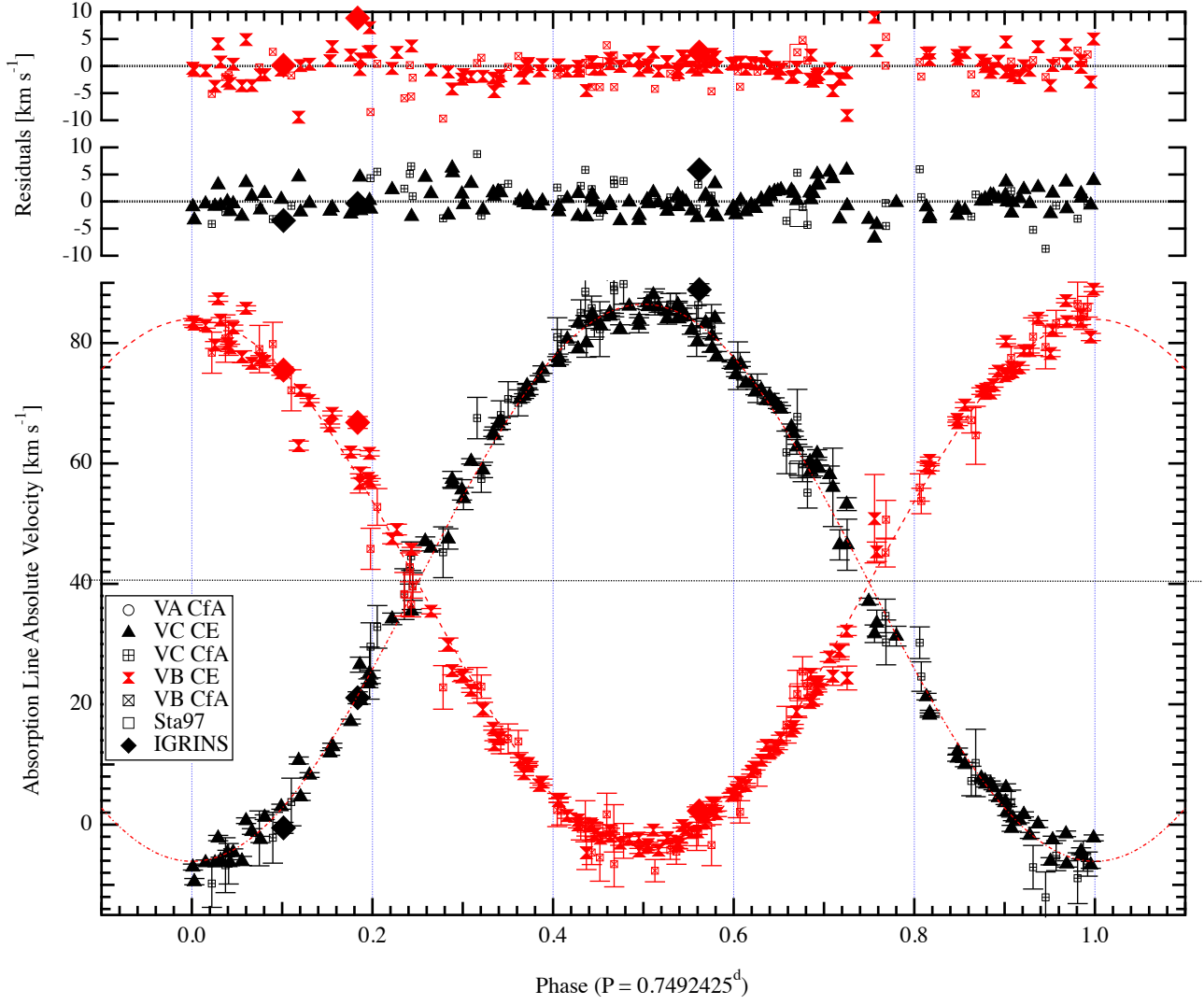


FIG. 2.— vA 351 absorption line radial velocities (Tables 3 and 4) for components B and C, phased to the BC period,  $P_{BC}$ . Orbital elements are given in Table 6. From the BC semi-amplitudes we derive a mass ratio  $\mathcal{M}_C/\mathcal{M}_B = 0.945 \pm 0.005$ . Also plotted are independent measures from IGRINS and Stauffer et al. (1997), where the errors have been estimated at  $1 \text{ km s}^{-1}$ .

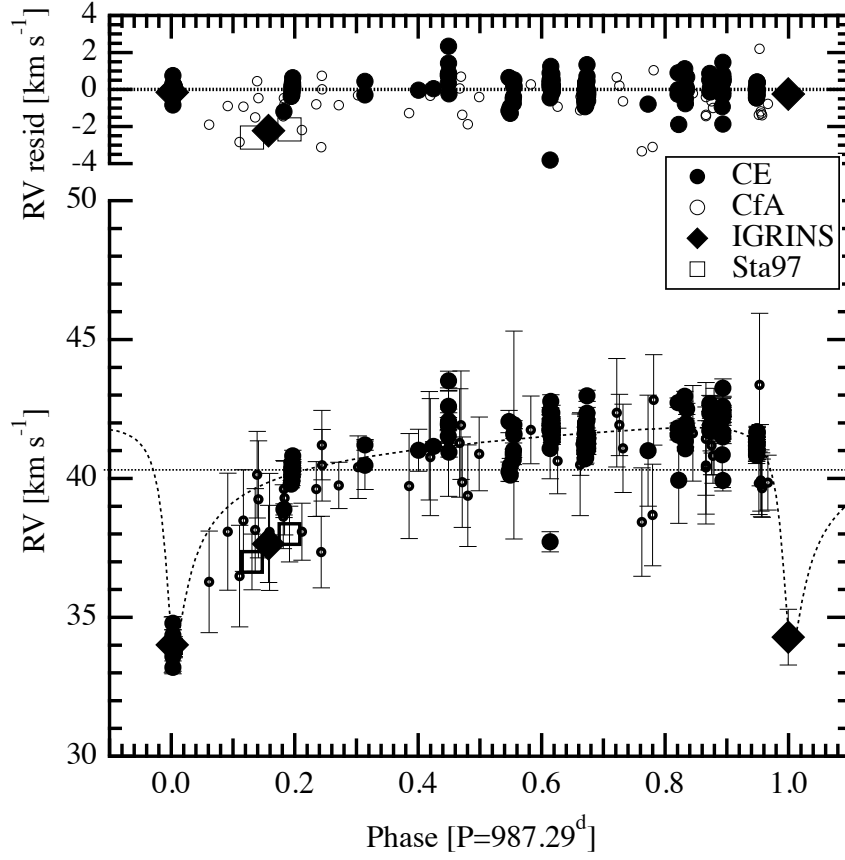


FIG. 3.— Radial velocities for component A plotted against phase of the AD-BC orbit (Section 3.4) obtained only from RVs. The horizontal line denotes the derived systemic velocity (Table 10).



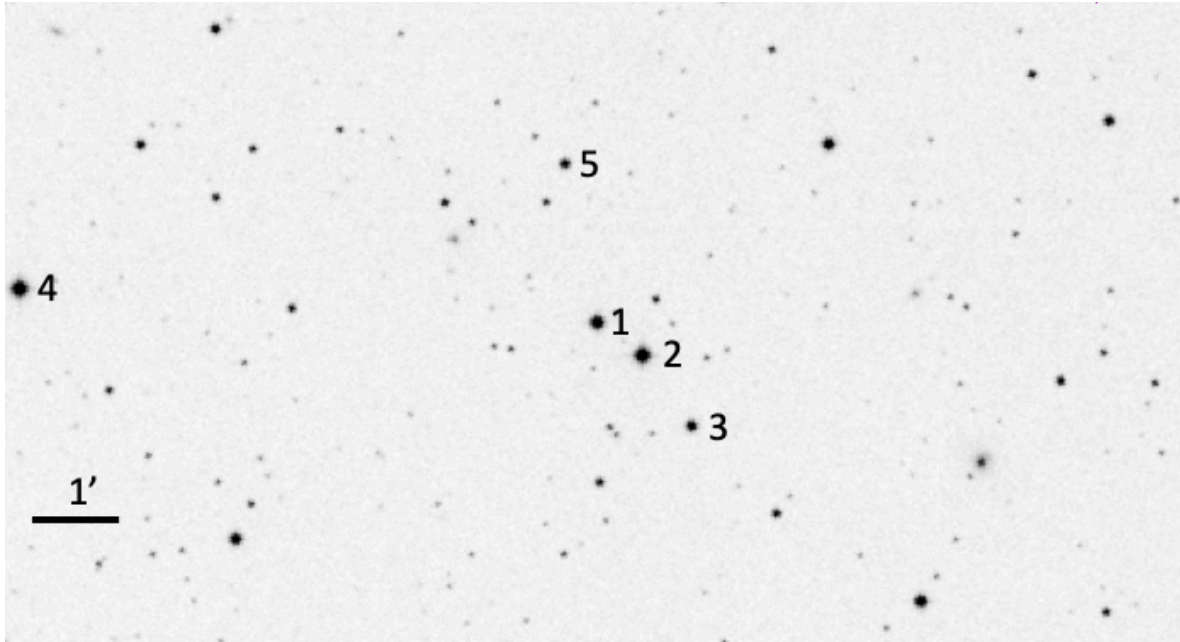


FIG. 4.— vA 351 and reference stars used in the POS mode astrometry; north at top, east at left. ID numbers from Table 8. The “1” indicates the location of the vA 351 photocenter. Image from Aladin.

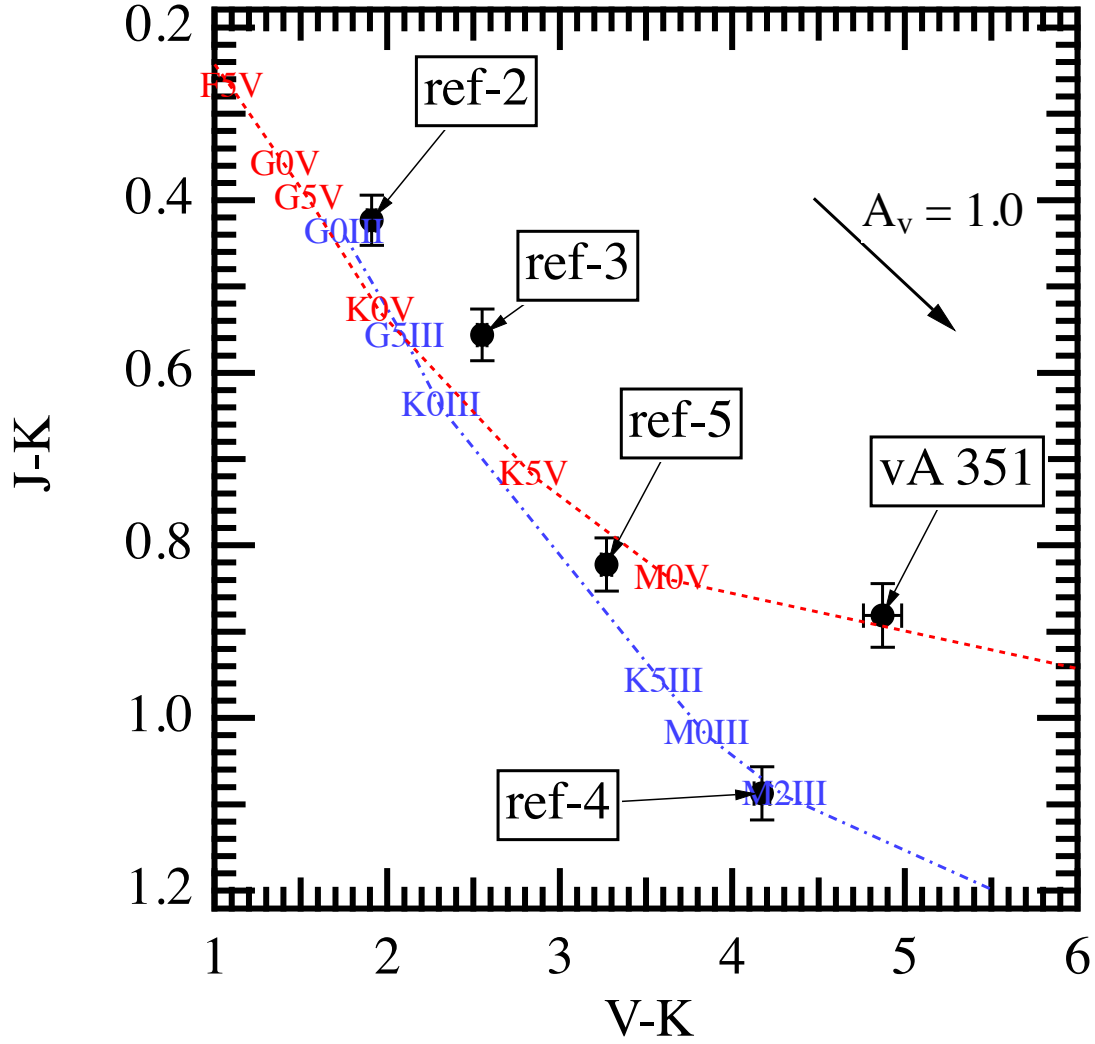


FIG. 5.—  $J - K$  vs.  $V - K$  color-color diagram for vA 351 and reference stars listed in Table 8. The dashed line is the locus of dwarf (luminosity class V) stars of various spectral types; the dot-dashed line is for giants (luminosity class III) from Cox (2000). The reddening vector indicates  $A_V=1.0$  for the plotted color systems. For this field at Galactic latitude  $\ell^{II} = -21^\circ$  we estimate  $\langle A_V \rangle = 1.4$ , midway between reddennings established for vA 310 and vA 383 in McArthur *et al.* (2011).

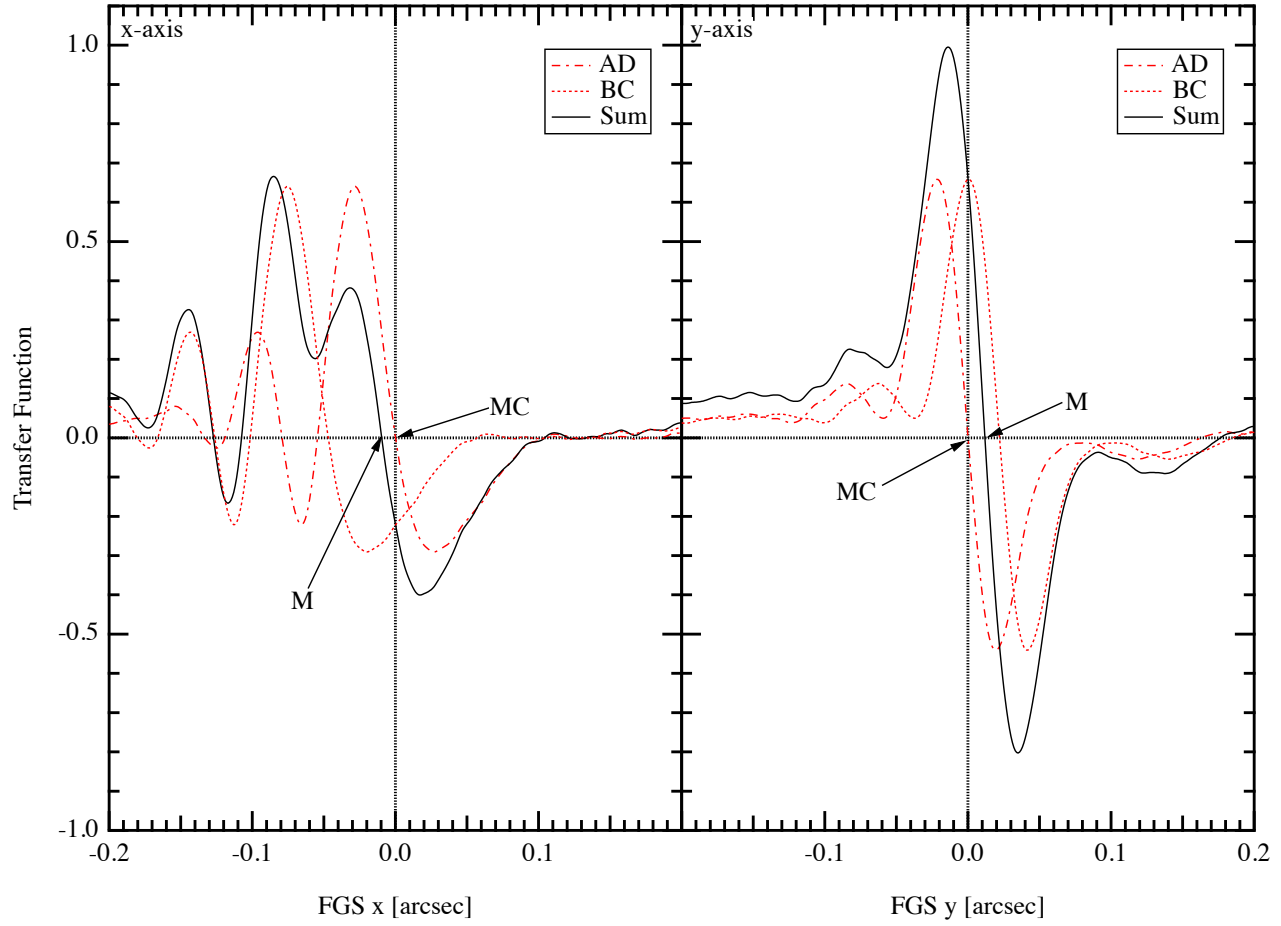


FIG. 6.— Given the very small brightness difference between components AD and BC, we apply photocenter corrections to the POS mode astrometry, which measures a zero-crossing for a sum of the two interferometric fringes. The arrow labeled M points to the position as measured by *FGS3*. The arrow labeled MC points to the actual position of component A. In each case the correction increases the separation between the components. The intrinsic fringe structure in the x-axis adds increased uncertainty to that correction. Corrections are +9 mas in x, -12 mas in y for  $\Delta m=0.0$ .

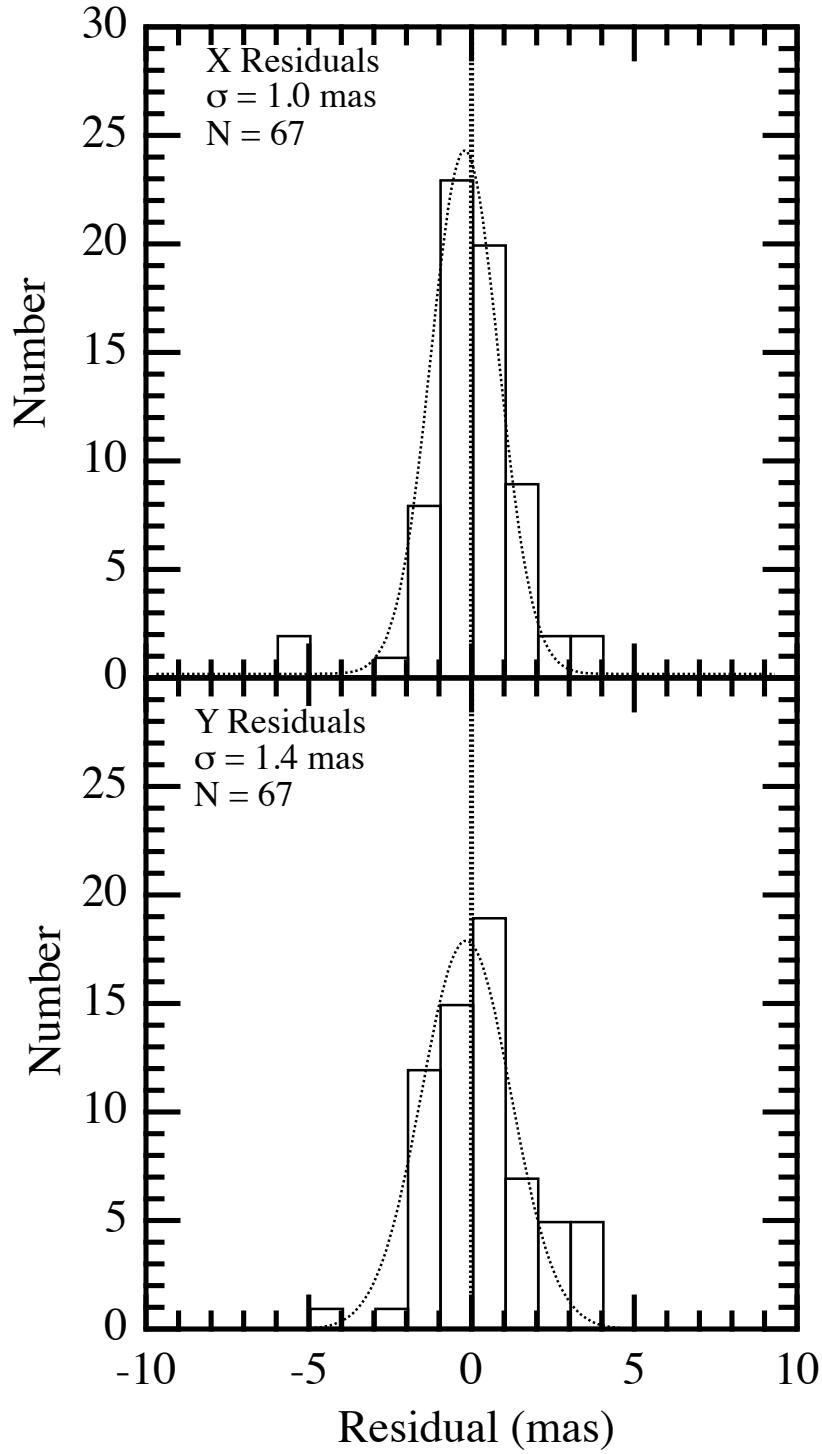


FIG. 7.— Histograms of  $\nu$ A 351 and reference star residuals resulting from the application of the astrometric model (Equations 5 and 6).

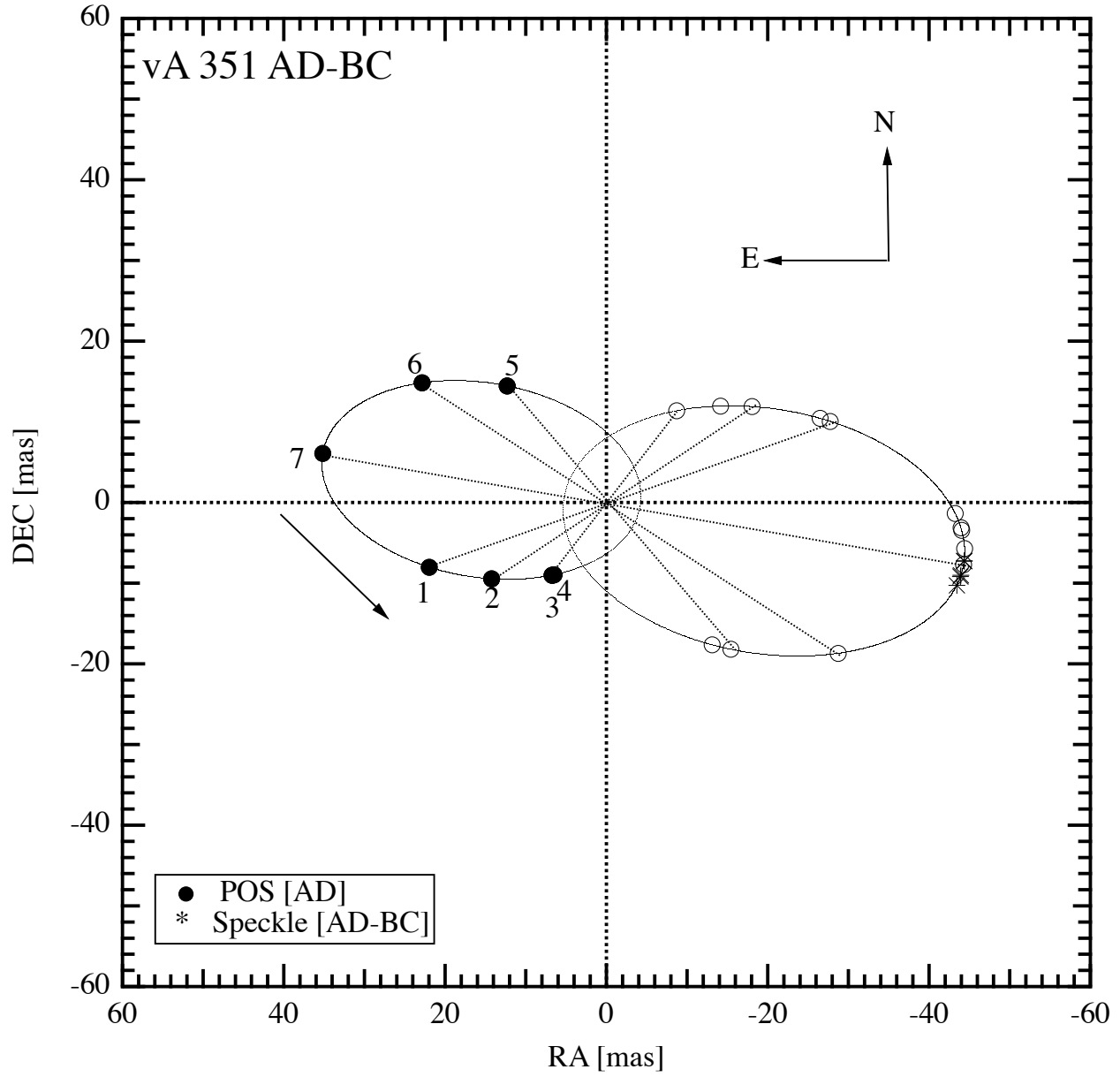


FIG. 8.— vA 351 component A (POS orbit calculated positions, ●) and component B (TRANS calculated, ○; speckle calculated, \*). POS measures the position of the AD combination relative to reference stars. TRANS measures the separations between and the position angles of AD relative to BC. All observations, speckle and TRANS, were used to derive the orbital elements listed in Table 10. POS measures yield only parallax, proper motion and mass fraction (Equation 9). The arrow indicates the direction of orbital motion.

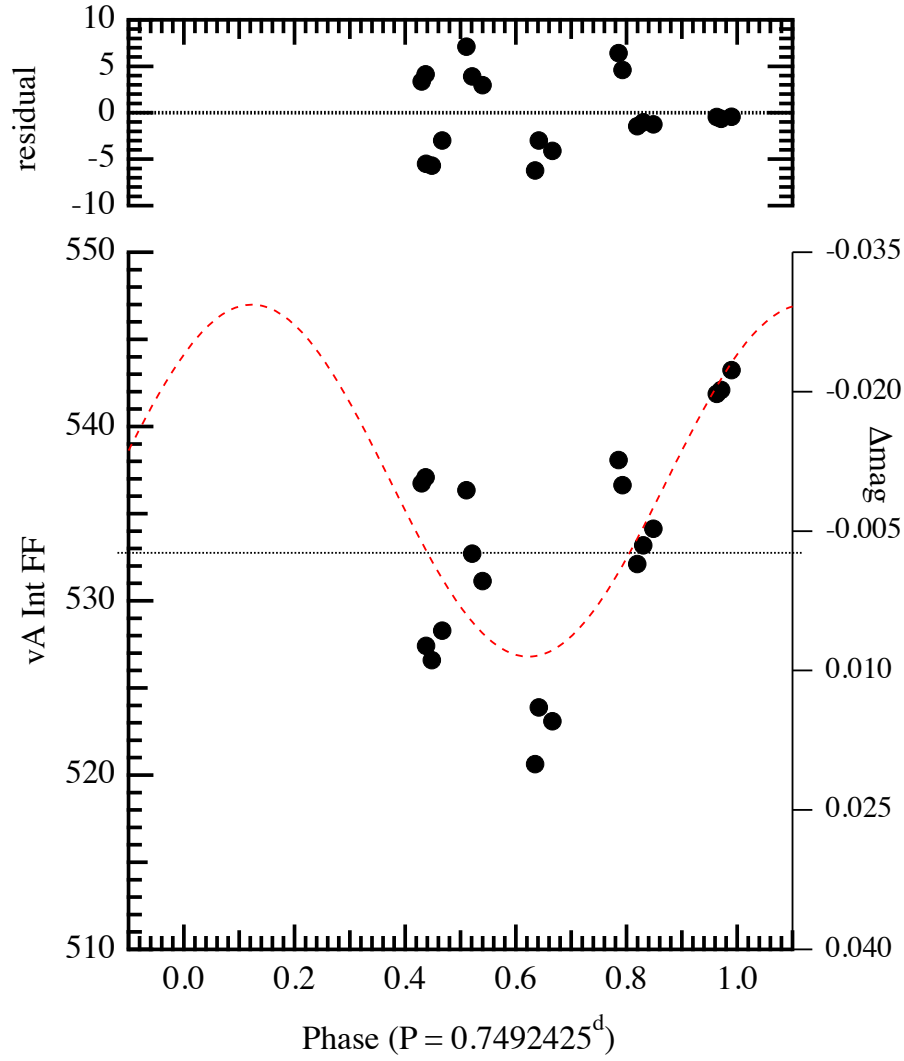


FIG. 9.— Flat-fielded vA 351 average counts from POS mode F583W photometry as a function of BC orbital phase. The *HST FGS* F583W filter includes  $H\alpha$ . The variation in magnitudes ( $\Delta\text{mag}$ ) is on the right. The fit is a sine wave with the period constrained to the BC orbital period, suggesting that the system is brighter when vA 351C is closest to us ( $\Phi_{\text{BC}} \sim 0.25$ ), and fainter when vA 351B is closest to us (at  $\Phi_{\text{BC}} \sim 0.75$ ), consistent with a small amount ( $\sim 0.01$  mag) of eclipse-induced dimming.

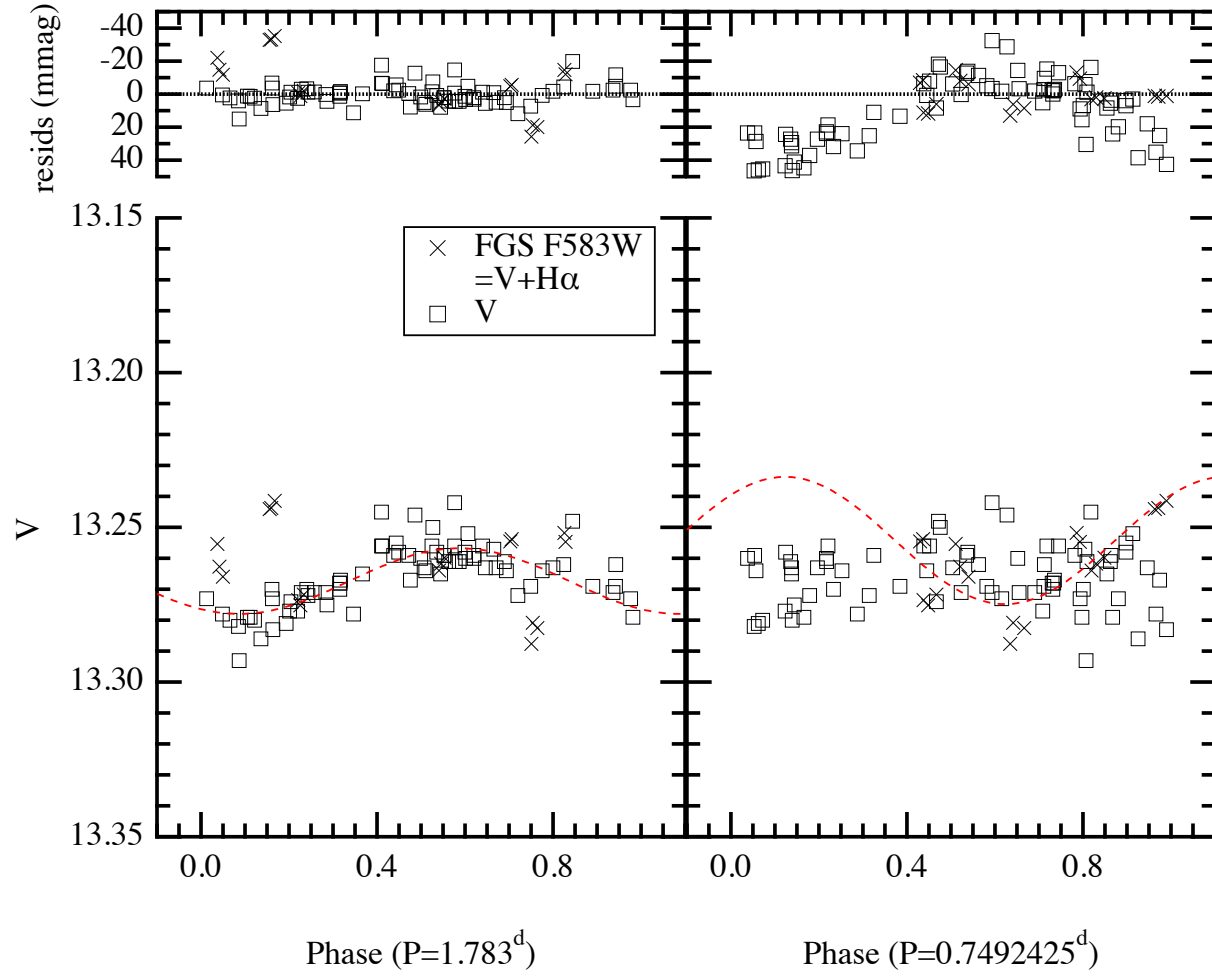


FIG. 10.— Left:  $V$ -band photometry ( $\square$ ) and  $FGS$  F583W photometry ( $\times$ ) phased to a period,  $P=1.783^d$ . Right: the same photometry phased to the BC orbital period with the fit from Figure 9.

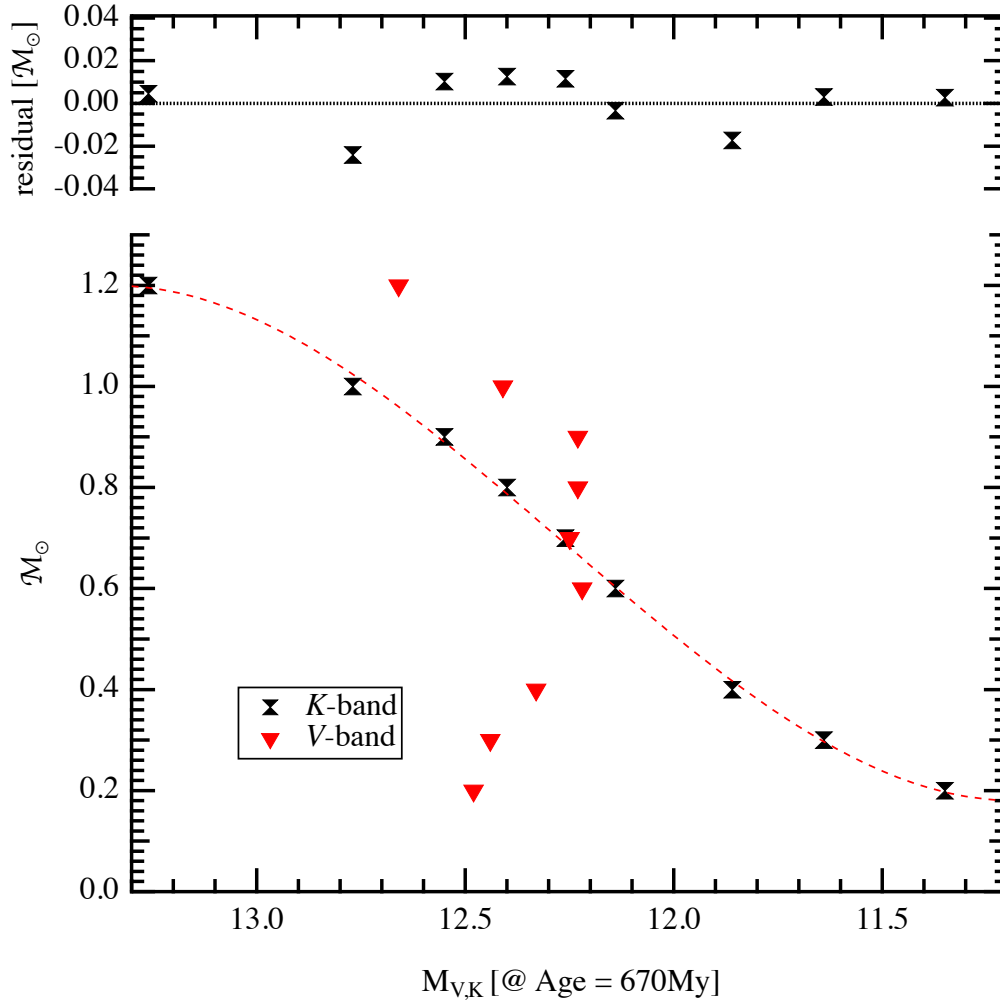


FIG. 11.— White dwarf mass in solar units ( $M_{\odot}$ ) as a function of  $K$ - and  $V$ -band absolute magnitude, derived from Bergeron cooling models, assuming a Hyades age of 670 My. We do not employ the multi-valued  $V$ -band relation as a constraint in the Section 6 component mass determination, but do use the  $K$ -band relation, fit with a third order polynomial with offset (coefficients in Table 12).



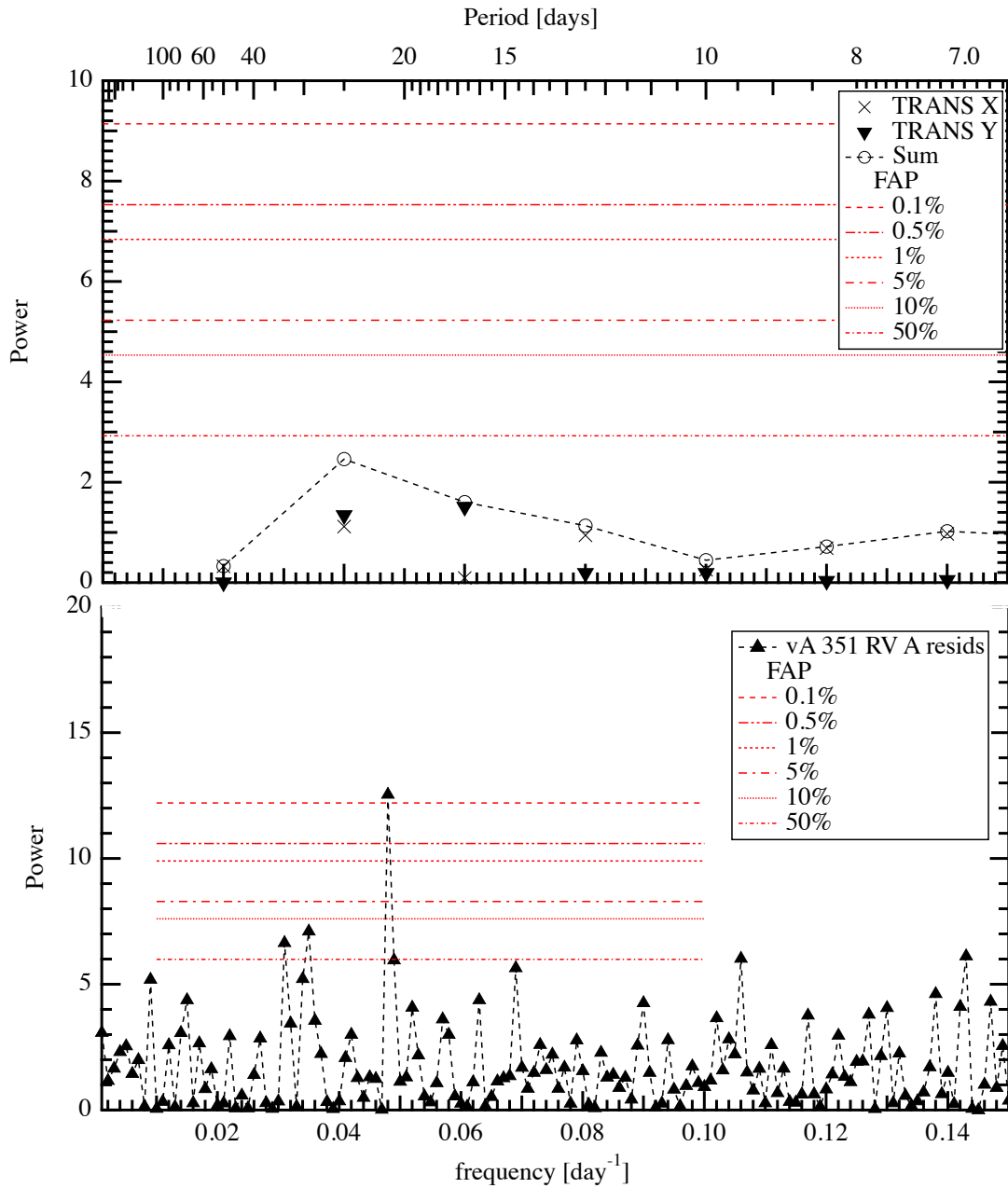


FIG. 12.— Bottom: Lomb-Scargle periodograms for the Figure 2 component A measured RV residuals, providing evidence (false-alarm probability of  $\sim 0.1\%$ ) for  $P_{\text{AD}} \sim 21^{\text{d}}$ . Top: periodograms of the TRANS mode and speckle X and Y residuals to the relative orbit (Figure 8). We also plot the sum of the X and Y power. They provide only weak support for a detection at  $P_{\text{AD}} \sim 25^{\text{d}}$ .

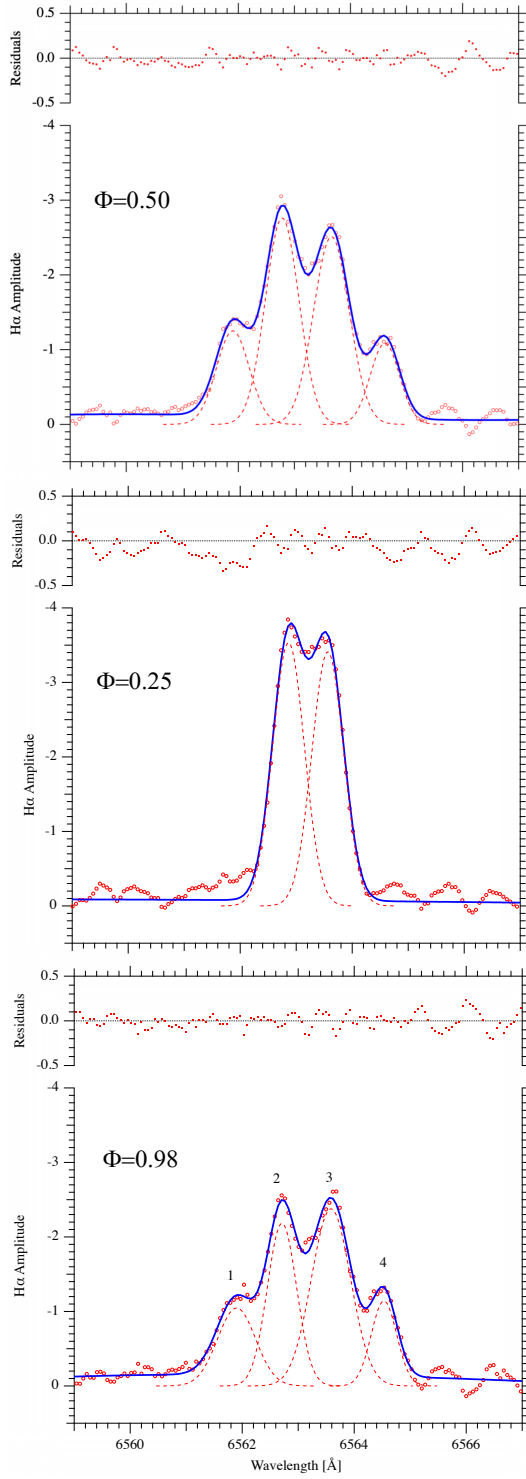


FIG. 13.— Structure in the  $H\alpha$  emission line amplitude ( $AW$ , Equation 12) at  $\Phi_{BC} = 0.50, 0.25, 0.98$ ; mJD=51467.36, 51466.42, 50724.47. In the bottom panel component B is the right-most peak, labeled 4; component C the left-most, labeled 1. In the top panel they have swapped sides because of BC orbital motion. In the middle panel components B and C partially fill-in the possible self absorption.

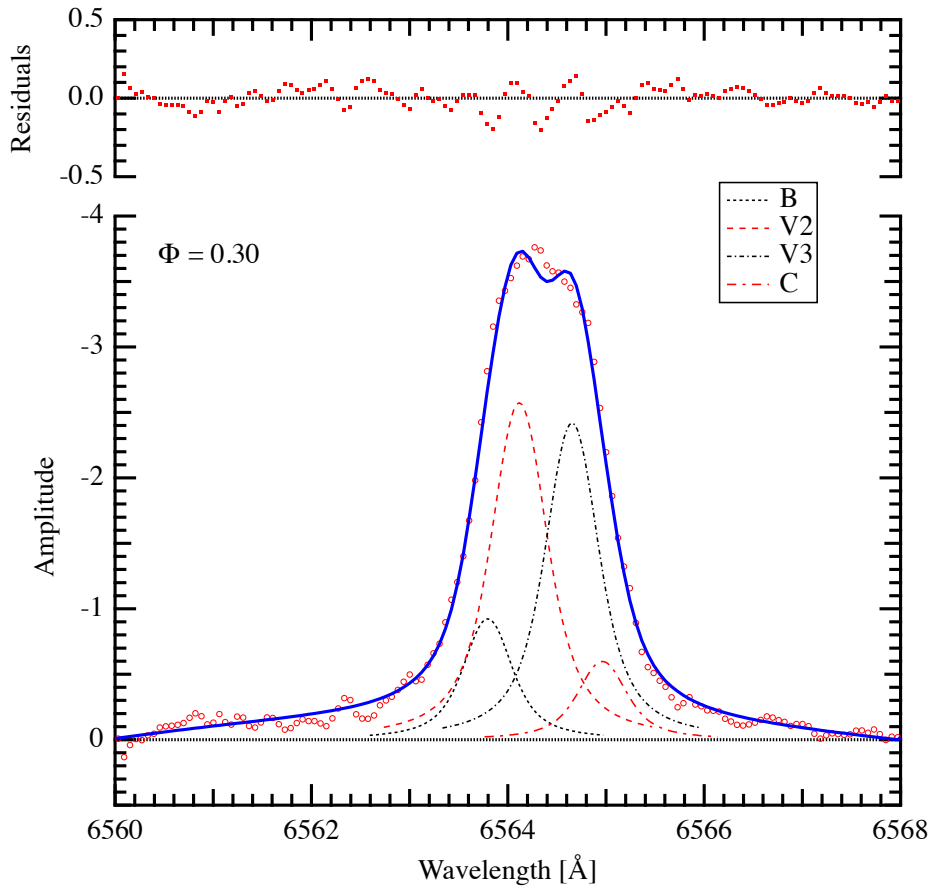


FIG. 14.— An example of extracting component B and C RVs for an observation near syzygy ( $\Phi = 0.30$ ) by constraining amplitude and width peak parameters to values measured for an observation at  $\Phi = 0.42$ , secured approximately two hours later that night. Using Voigt functions, the model solves only for component positions in wavelength.

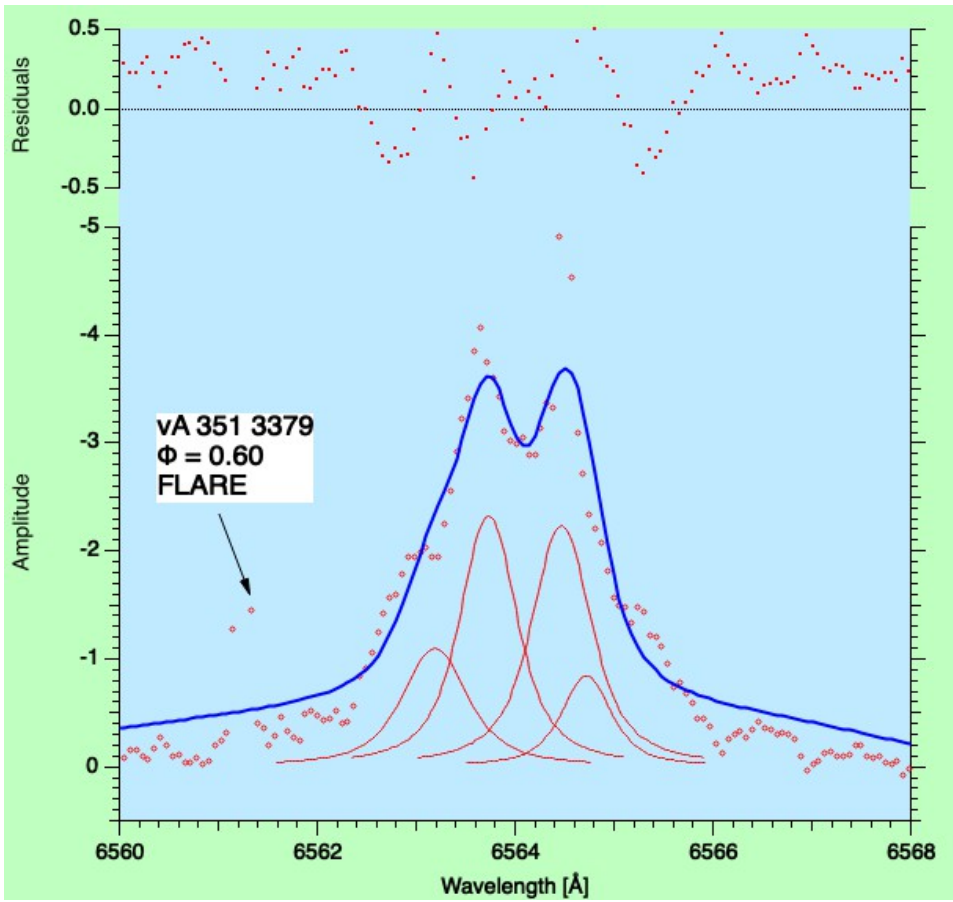


FIG. 15.— An animated version of Figure 13, showing the behavior of  $H\alpha$  as a function of BC orbital period. This particular frame (observation date  $mJD=51193.2104$ ) exhibits flaring activity associated with components 2 and 3 identified in Figure 13. The number next to the vA 351 identification is a running RV observation log number.  $\Phi$  indicates BC orbital phase. The animation is constructed from data acquired with the CE, spanning a range  $50723 < mJD < 52948$ .

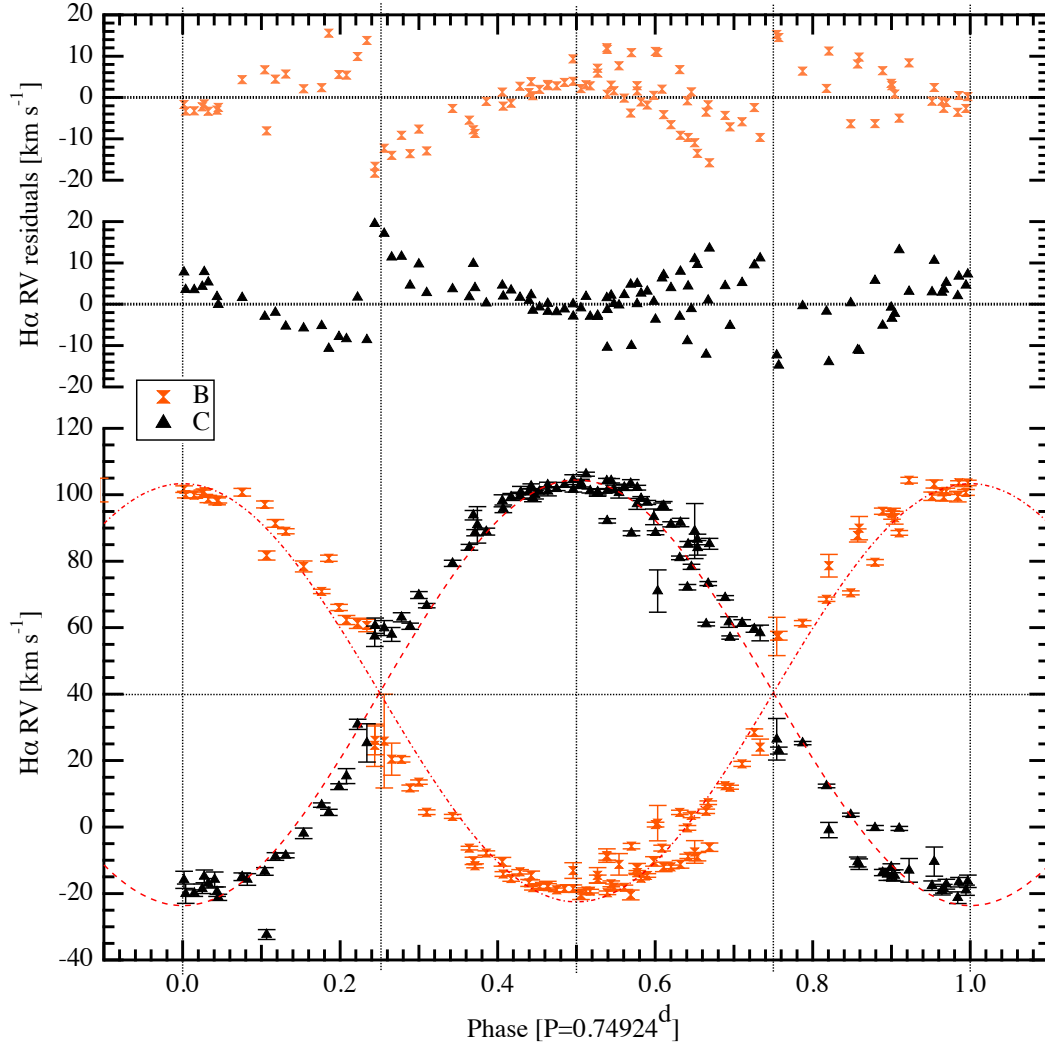


FIG. 16.— vA 351 H $\alpha$  radial velocities for components B and C (peaks 4 and 1 in Figure 13) phased to the period derived from absorption lines (Figure 2). Vertical lines indicate quadrature (phases  $\Phi_{BC} = 0.0, 0.5, 1.0$ ) and syzygy (phases  $\Phi_{BC} = 0.25, 0.75$ ). The amplitude derived from H $\alpha$  significantly exceeds the amplitude exhibited by absorption lines (Figure 2, Table 6). Residuals indicate unmodeled non-circular motions in H $\alpha$ .

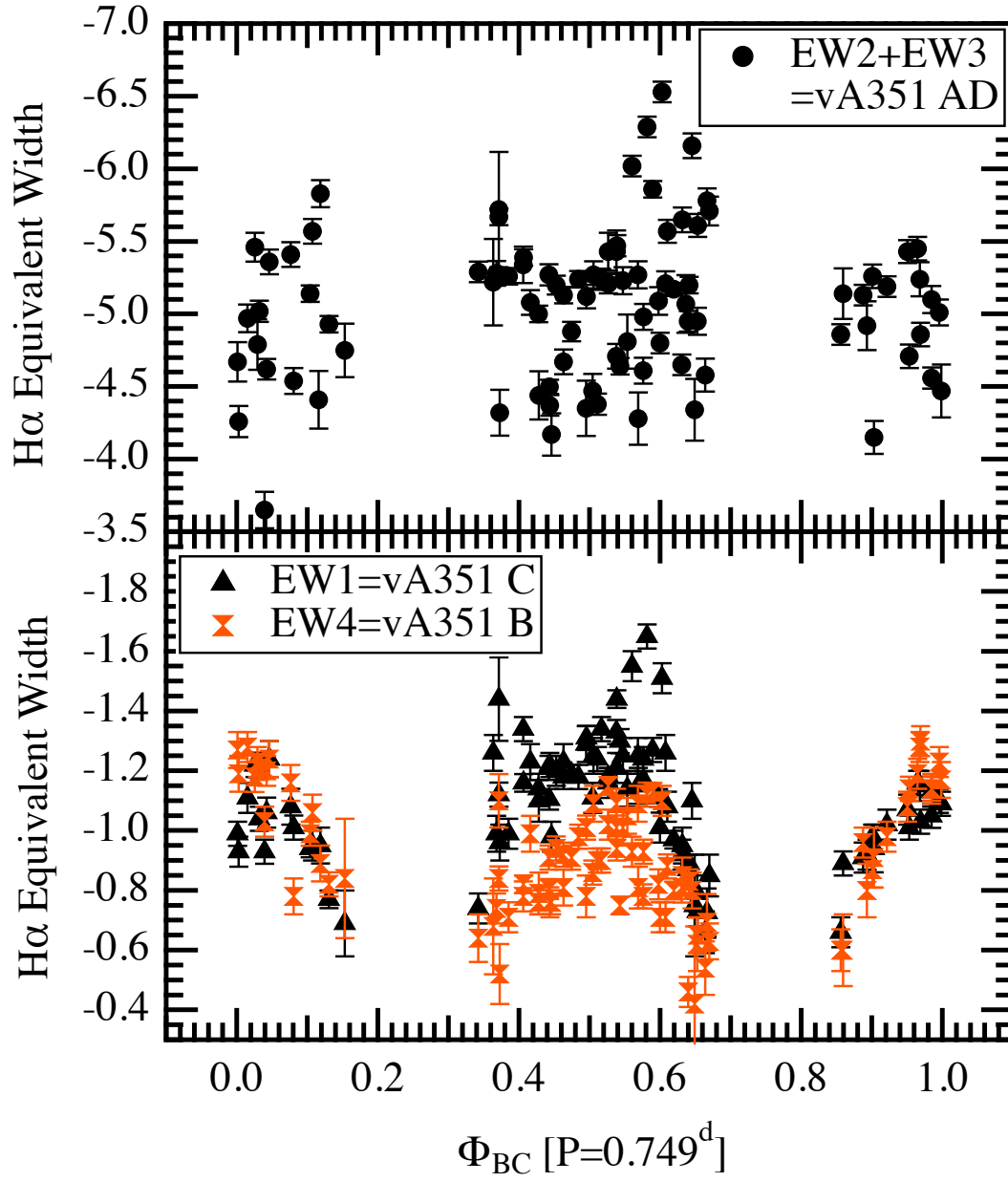


FIG. 17.— H $\alpha$  equivalent widths for, bottom, components B and C, top, the sum of components 2 and 3, phased to the orbital period derived from absorption line velocities (Figure 2). Values are only for  $0.35 \leq \Phi_{BC} \leq 0.65$ ,  $0.85 \leq \Phi_{BC} \leq 1.00$ , and  $0.00 \leq \Phi_{BC} \leq 0.15$  to minimize contamination between components. H $\alpha$  emission from components B and C correlate with the BC period. The sum of components 2 and 3 do not, supporting their association with vA 351A and D.

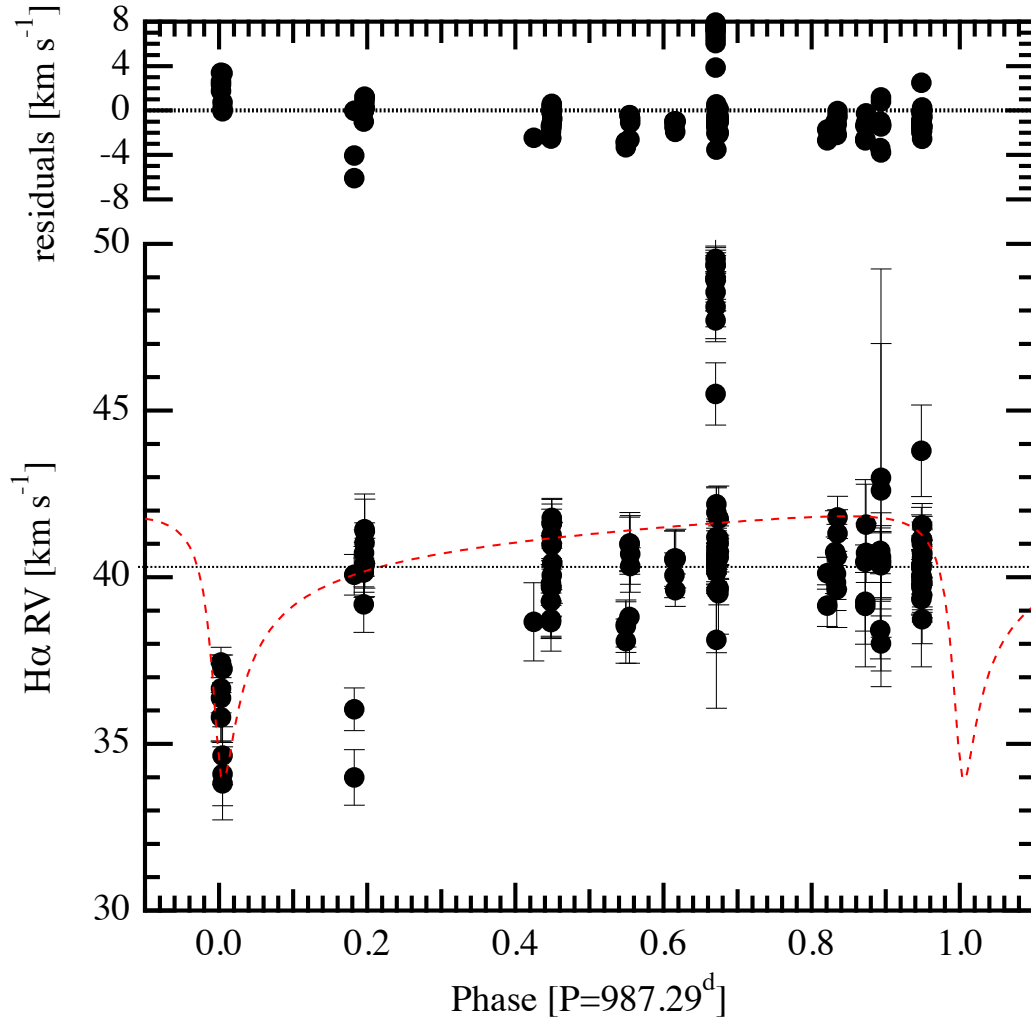


FIG. 18.— vA 351 H $\alpha$  RVs for an average of components 2 and 3 (identified in Figure 13) phased to the period (Table 10) derived from absorption line RVs and the relative orbit. The Figure 3 AD-BC RV orbit is overplotted. While noisy, RVs suggest that components 2 and 3 of the H $\alpha$  emission have an association with components AD.

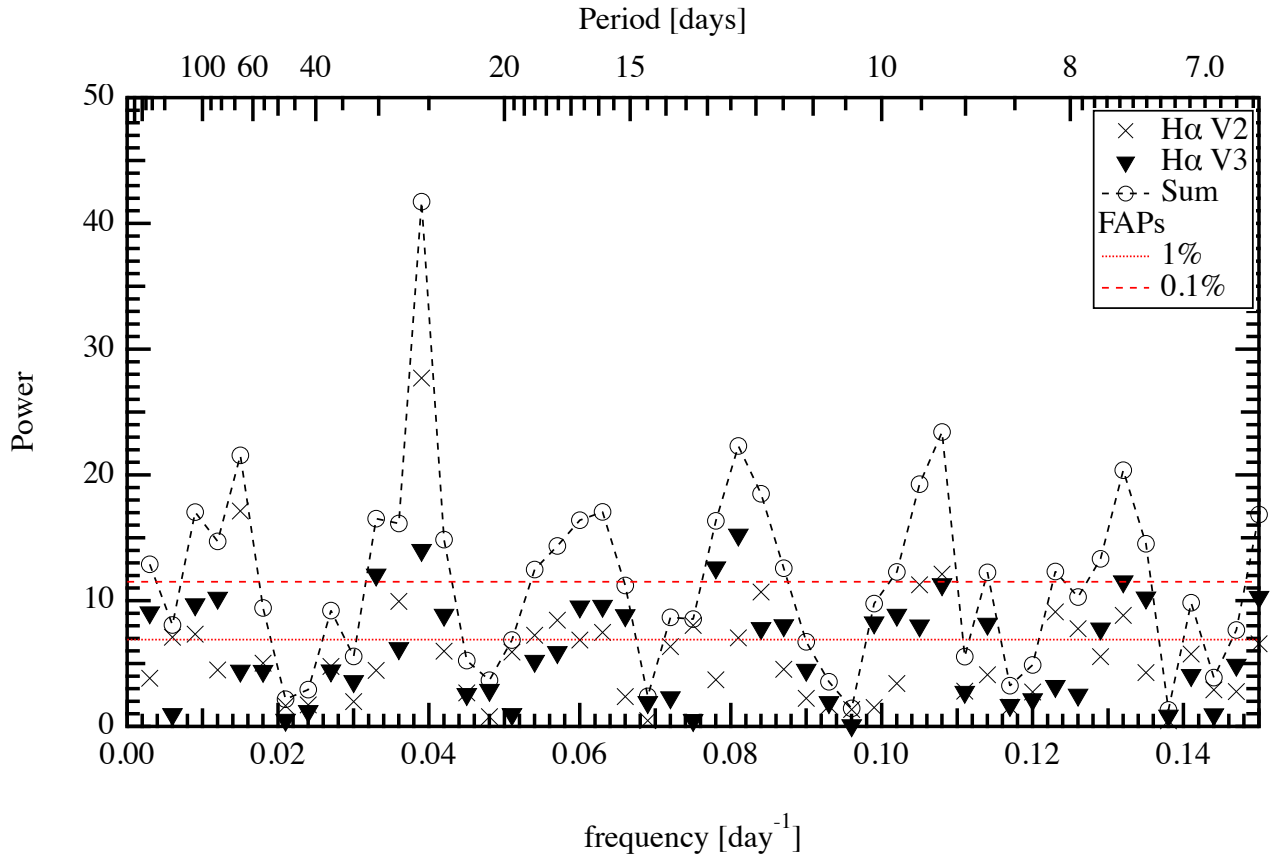


FIG. 19.— Lomb-Scargle periodograms for the Figure 13 H $\alpha$  V2 and V3 components and the periodogram sum, providing significant evidence (false-alarm probability  $\ll 0.1\%$ ) for activity with  $P_{\text{AD}} \sim 25^{\text{d}}$ . This provides supporting evidence for the reality of the astrometric and RV detections at  $P_{\text{AD}} \sim 21^{\text{d}}$  (Figure 12).



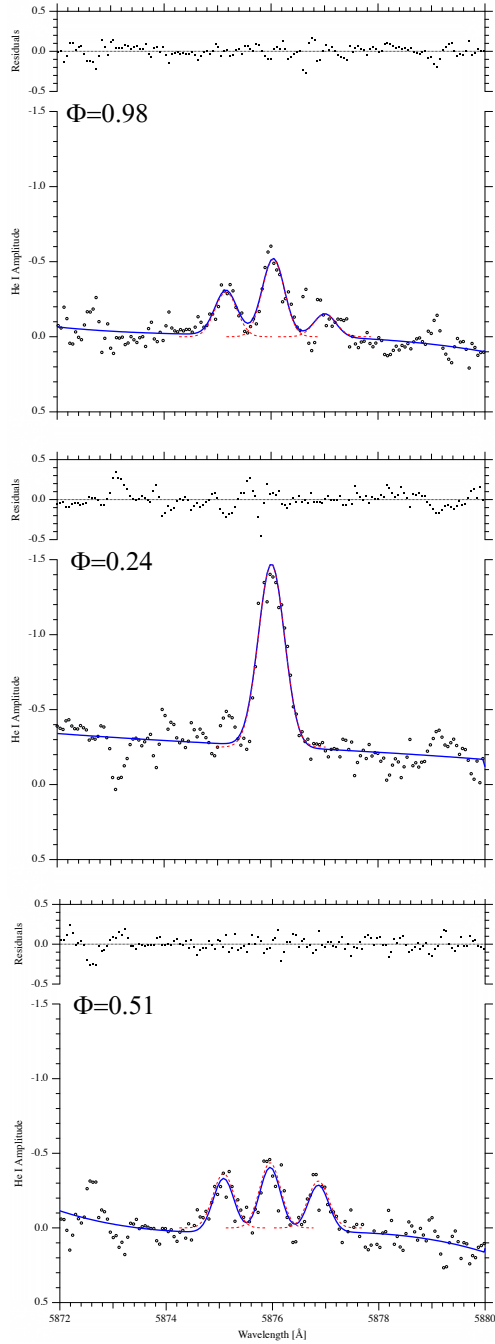


FIG. 20.— Structure in the He I emission line ( $\lambda 5875\text{\AA}$ ) amplitude ( $AW$ , Equation 12) from bottom to top at  $\Phi_{BC} = 0.51, 0.24, 0.98$ ;  $mJD = 51467.36, 51466.42, 50724.47$ . At phase  $\Phi_{BC} = 0.51$  component C is the right-most peak; component B the left-most. There is no central peak structure at any phase. Tables 16 and 17 list EW and RVs for these and other observations. The emission is far weaker (factors of 2-6), thus the S/N lower, than for the  $H\alpha$  (Figure 13) from the same spectra. The broad Na D absorption line at  $\lambda 5889.9\text{\AA}$  produces the sloping background.

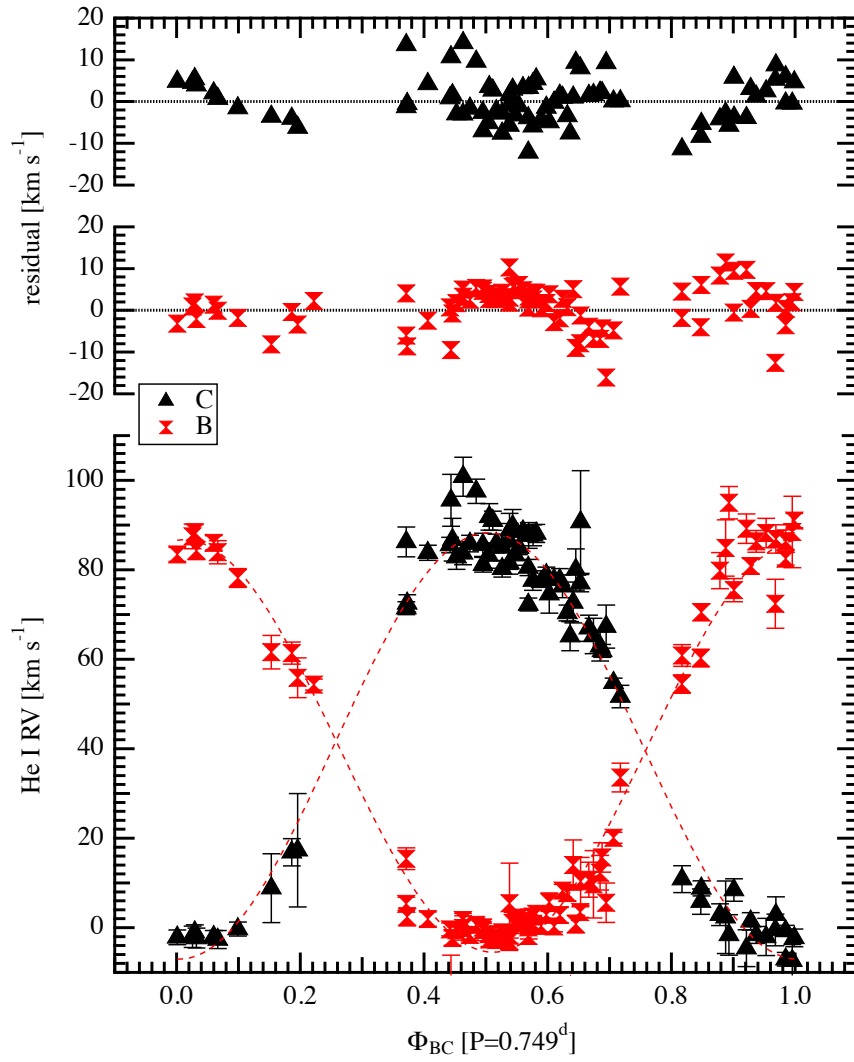


FIG. 21.— He I ( $\lambda 5875\text{\AA}$ ) emission line radial velocities for components B and C phased to the period derived from absorption lines (Figure 2). Emission peak fitting provides all velocities. Scatter is larger than for absorption or H $\alpha$  measures. Amplitudes,  $K$ , and systemic velocity,  $\gamma$ , (Table 6) have values closer to those from absorption line velocities.

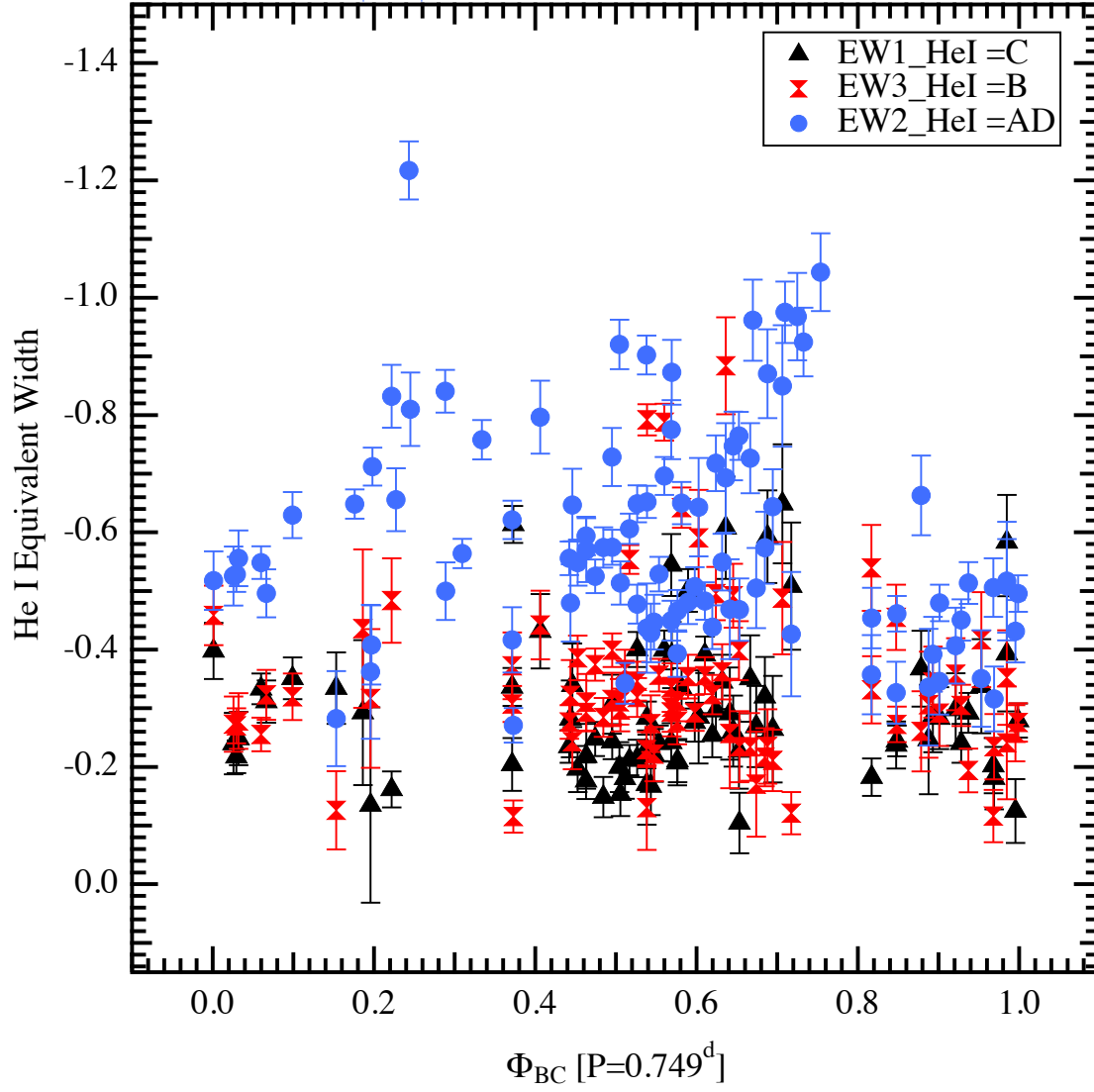


FIG. 22.— He I equivalent widths for components A, B and C phased to the orbital period derived from absorption line velocities (Figure 2). He I emission from components A, B, and C show little correlation with the BC period.

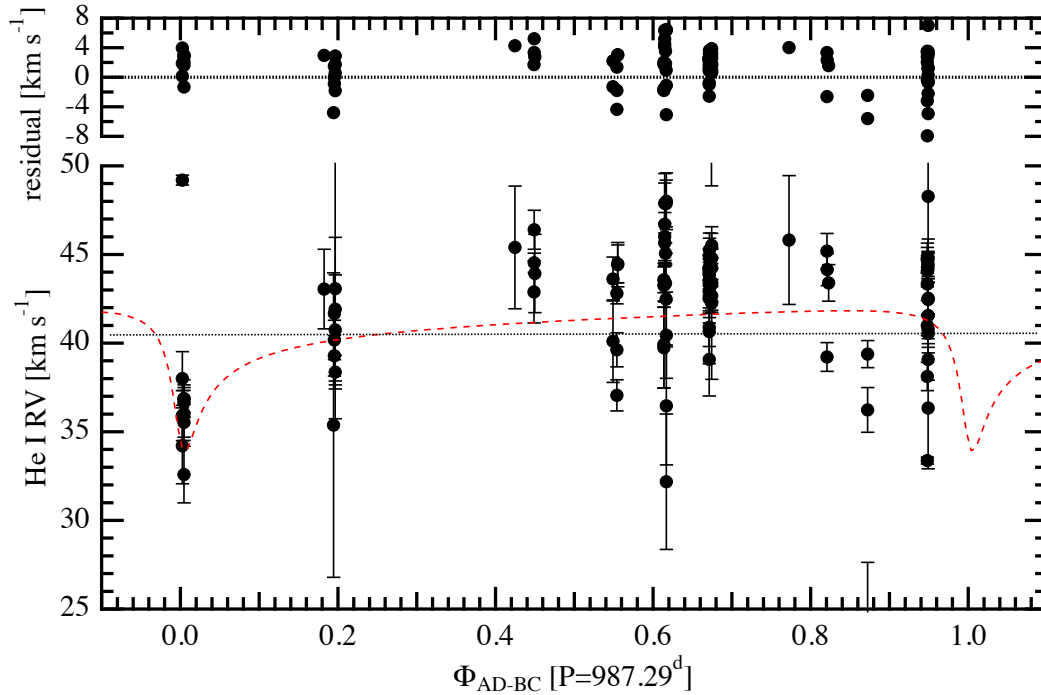


FIG. 23.— vA 351 He I RVs for the central peak emission (Figure 14) phased to the AD-BC period (Table 10) derived from absorption line RVs and the relative orbit. The Figure 3 orbit is overplotted. While noisy, velocities suggest that the central component of the He I emission is associated with components AD.

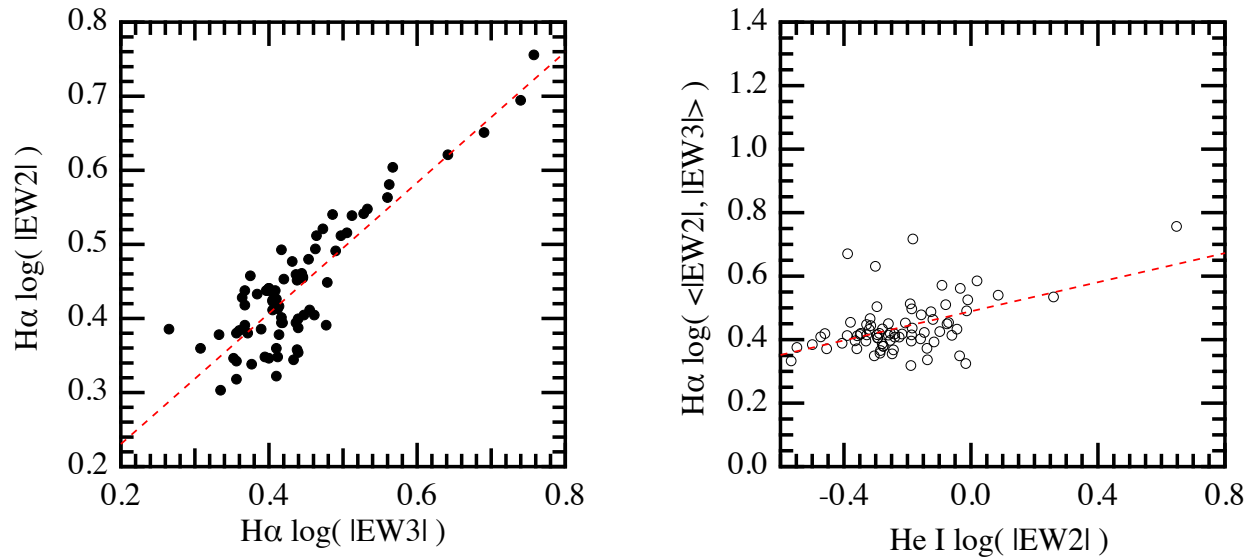


FIG. 24.— Left: log of the absolute values of EW2 versus EW3 (Table 13, peaks 2 and 3 in Figure 13). The maximum values occur within 4 days of AD-BC orbit periastron. Right: log of the average absolute values of EW2 and EW3 versus the log of the absolute value of the He I central peak ( $EW_{\text{cen}}$ , Table 16; central peak in Figure 20). The correlation (Pearson's  $r$  value,  $Pr = 0.49$ ) only weakly supports the assertion that the same energy source powers the H $\alpha$  and He I activity. The strongest values for a few of the H $\alpha$  EW2, EW3 averages, but only one He I epoch, occur within 4 days of AD-BC periastron.

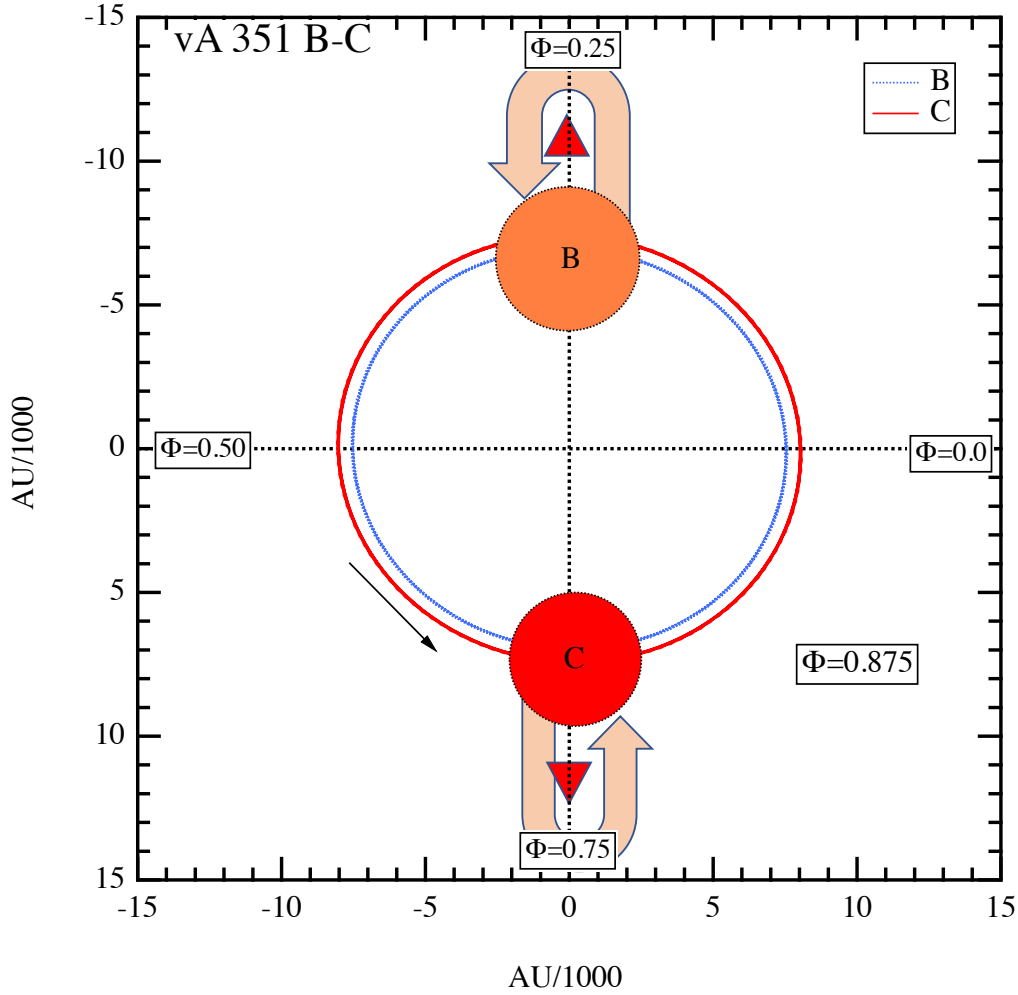


FIG. 25.— A cartoon of the vA 351 BC components, scaled to AU using knowledge of the component masses, absorption line RV amplitudes ( $K_B$  and  $K_C$ ), the system parallax, and Kepler's Laws. We adopt component stellar sizes from the Boyajian et al. (2012) mass-radius relation for eclipsing binaries. The fatter colored tracks represent coronal loop-like flows that could explain the  $H\alpha$  RV residual patterns in Figure 16. The arrows are notional, not to scale, only indicating flow direction.  $H\alpha$  emission takes place in the darker triangles, parts of the flow most shaded from the other component. Those locations are to scale. Phases,  $\Phi$ , match Figures 2 and 16. The He I  $K$  values (Figure 23, Table 6) match those from absorption lines, so He I emission is likely produced nearer the stellar surface. The He I RV residuals (Figure 21), while far noisier, suggest a flow pattern similar to that of  $H\alpha$ .

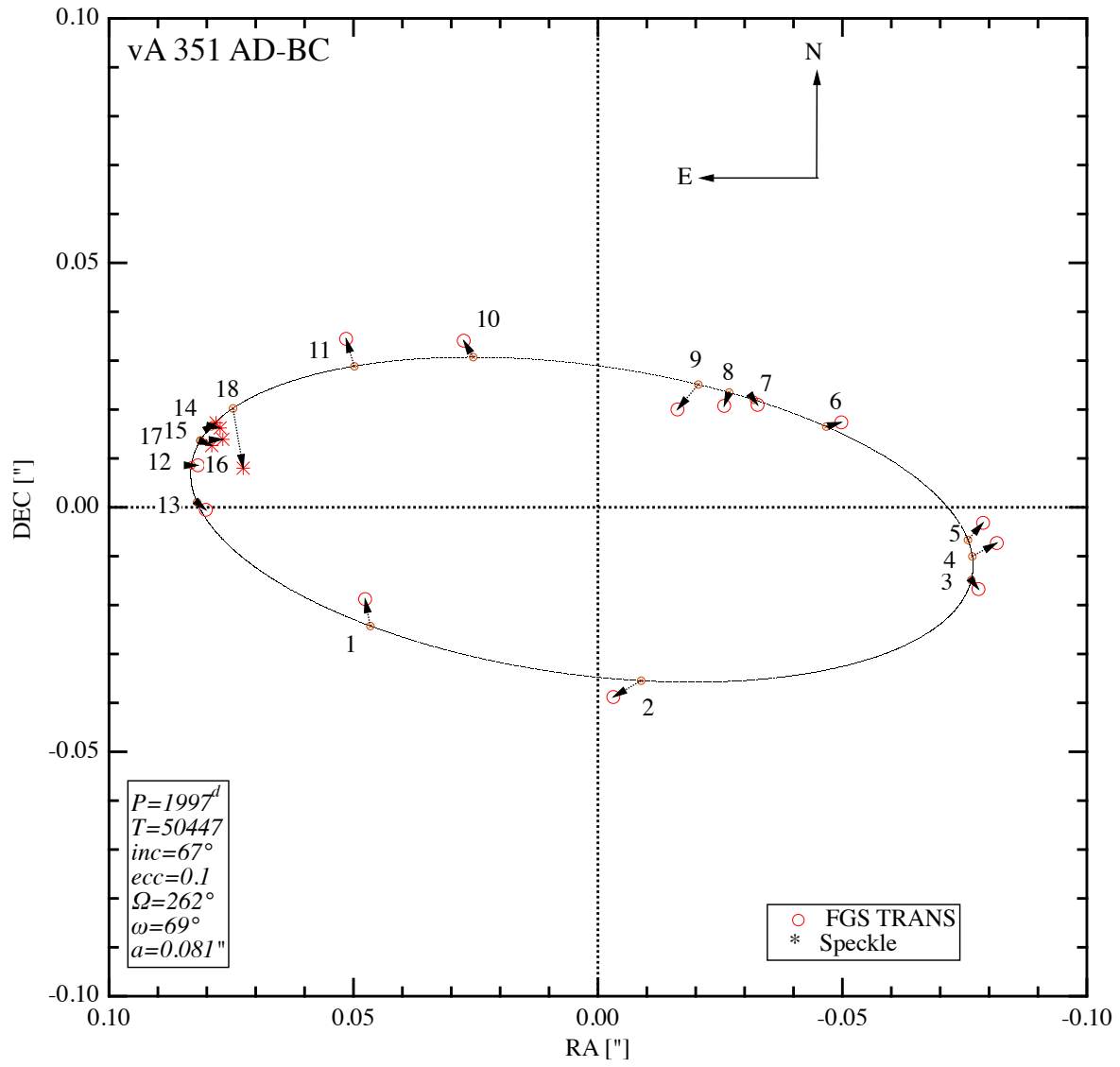


FIG. 26.— Misidentification of nearly equal and variable brightness components result in this relative orbit AD-BC for vA 351 derived from FGS TRANS and ground-based speckle observations. Compare with Figure 1.